Neutralizing human monoclonal antibodies that target the PcrV component of the Type III Secretion System of *Pseudomonas aeruginosa* act through distinct mechanisms

Jean-Mathieu Desveaux[1], Eric Faudry[1], Carlos Contreras-Martel[1], François Cretin[1], Leonardo Sebastian Dergan-Dylon[1], Axelle Amen[1,2], Isabelle Bally[1], Victor TardivyCasemajor[1], Fabien Chenavier[1], Delphine Fouquenet[3], Yvan Caspar[1,4], Ina Attrée*[1], Andréa Dessen*[1], Pascal Poignard*[1,5]

[1] Univ. Grenoble Alpes, CEA, CNRS, Institut de Biologie Structurale (IBS), F-38044 Grenoble, France

[2] Laboratoire d'Immunologie, CHU Grenoble Alpes, France

[3] Centre d'Étude des Pathologies Respiratoires INSERM U1100 - UFR de Médecine de Tours, 10 Bd Tonnellé, 37032 Tours Cedex

[4] Laboratoire de Bactériologie-Hygiène Hospitalière, CHU Grenoble Alpes, France

[5] Laboratoire de Virologie, CHU Grenoble Alpes, France

* to whom correspondence should be addressed: ina.attree@ibs.fr, andrea.dessen@cnrs.fr, pascal.poignard@ibs.fr

ABSTRACT

Pseudomonas aeruginosa is a major human opportunistic pathogen associated with a high incidence of multi-drug resistance. The antibody-based blockade of *P. aeruginosa* virulence factors represents a promising alternative strategy to mitigate its infectivity. In this study, we employed single B cell sorting from cystic fibrosis patients to isolate human monoclonal antibodies (mAbs) targeting proteins from the *P. aeruginosa* Type 3 Secretion System (T3SS) and characterized a panel of mAbs directed at PscF and PcrV. Among those, two mAbs, P5B3 and P3D6, that bind to the injectisome tip protein PcrV, exhibited T3SS blocking activity. We solved the crystal structure of the P3D6 Fab-PcrV complex, which revealed that the Ab binds to the C-terminal region of PcrV. In addition, we compared the T3SS-blocking activity of three PcrV-targeting mAbs, including two from previous independent studies, using two distinct assays to evaluate pore formation and toxin injection. We conducted a mechanistic and structural analysis of their modes of action through modeling based on the known structure of a functional homolog, SipD from *Salmonella typhimurium*. The analysis suggests that anti-PcrV mAbs may act through different mechanisms, ranging from preventing PcrV oligomerization to disrupting PcrV's scaffolding function, thereby inhibiting the assembly and function of the translocon pore. Our findings provide additional evidence that T3SS-targeting Abs, some capable of inhibiting virulence, are elicited in *P. aeruginosa*-infected patients. The results offer deeper insights into PcrV recognition by mAbs and their associated mechanisms of action, helping to identify which Abs are more likely to be therapeutically useful based on their mode of action and potency. This paves the way for the development of effective alternatives to traditional antibiotics in the fight against this resilient pathogen.

52 **INTRODUCTION**

53 The emergence of antimicrobial resistance is a major threat to human health.
54 Among the microorganisms whose resistance rates have increased the most
55 dramatically are ESKAPE pathogens (***E****nterococcus faecium,* ***S****taphylococcus aureus,*
56 ***K****lebsiella pneumoniae,* ***A****cinetobacter baumannii,* ***P****seudomonas aeruginosa,*
57 ***E****nterobacter spp*) for which novel antibacterial treatments are urgently needed.
58 However, an antibiotic discovery hiatus that occurred during the last few decades
59 severely heightened the resistance threat (Murray et al., 2022), underlining the
60 importance of exploring alternative strategies such as host-targeting, bacteriophage,
61 anti-virulence, and Ab-based therapies (De Melo et al., 2024; Kaufmann et al., 2018;
62 Morrison, 2015).

63 Therapeutic mAbs have been successfully developed to fight viral infections
64 ranging from Ebola to SARS-CoV-2 (Crowe, 2022; Levin et al., 2022; Mulangu et al.,
65 2019). To date, however, only three therapeutic Abs have been marketed against
66 bacteria, all of which target toxins. Other types of bacterial virulence factors could also
67 serve as potential high importance targets for mAbs. Recent examples include the
68 development of mAbs that target lipopolysaccharides, O-antigen, and outer membrane
69 transporter proteins, notably in *Klebsiella pneumoniae* and *Mycobacterium*
70 *tuberculosis* (Pennini et al., 2017; Rollenske et al., 2018; Watson et al., 2021). The
71 advantages of targeting virulence factors through mAbs include notably a high
72 specificity and the decreased likelihood of the emergence of resistance among bacteria
73 (La Guidara et al., 2024). Additionally, the employment of mAb engineering platforms
74 offers the potential for improved efficacy through modifications such as half-life
75 extension and alterations of Fc effector functions (Morrison, 2015; Vacca et al., 2022).
76 Finally, strategies such as the use of mAb cocktails targeting different specificities and
77 the combination with traditional antibiotics further expand the range of Ab-based
78 treatment options (Duan et al., 2021; Morrison, 2015; Tabor et al., 2018).

79 *Pseudomonas aeruginosa* is a major nosocomial pathogen and the leading
80 cause of acute pneumonia and chronic lung infections, particularly in ventilatorassisted
81 and cystic fibrosis (CF) patients. Infections with *P. aeruginosa* ultimately lead to loss of
82 lung function and death in CF patients. Worldwide, *P. aeruginosa* is responsible for
83 more than 300,000 deaths associated or attributed to resistance each year. The natural

resistance of *P. aeruginosa* to a broad range of antibiotics, its ability to grow as biofilms, as well as its widespread presence in hospital settings (Horcajada et al., 2019; Murray et al., 2022), have called for urgent efforts towards the development of new therapeutic agents. Aggressive acute infections by *P. aeruginosa* are highly dependent on its Type III Secretion System (T3SS), a needle-like, multicomponent secretion machinery located on the cell surface and that transports effectors from the bacterial cytoplasm directly into the host cell cytosol (Goure et al., 2004; Hauser, 2009; Quinaud et al., 2007, 2005). It is of note that in other human pathogens such as *Yersinia pestis*, *Salmonella typhi*, *Shigella dysenteriae* and *Escherichia coli* the T3SS also plays a key role in virulence, participating in the causation of diseases such as plague, typhoid fever, and bacillary dysentery, respectively (Coburn et al., 2007; Diepold and Wagner, 2014; Hu et al., 2017; Serapio-Palacios and Finlay, 2020).

A key component of the T3SS is the injectisome, membrane-embedded protein rings extended by a hollow needle, composed of the PscF protein that protrudes outwards from the bacterial surface. Injectisome-dependent toxin delivery, which occurs upon contact with the eukaryotic target cell, also requires formation of the 'translocon', a complex of three proteins that are exported through the interior of the polymerized needle, assemble at its tip and form a pore in the eukaryotic cell membrane, an essential step for effector injection (Mueller et al., 2008). The translocon is composed of two hydrophobic proteins (PopB and PopD in *P. aeruginosa*), as well as a hydrophilic partner - PcrV, or the V antigen- in *P. aeruginosa* (Matteï et al., 2011). PopB and PopD have been shown to act as *bona fide* pore-forming toxins (Schoehn et al., 2003; Faudry et al., 2006; Montagner et al., 2011) that, upon membrane disruption, can trigger the manipulation of host processes including histone dephosphorylation and mitochondrial network disruption (Dortet et al., 2018). PcrV, on the other hand, oligomerizes at the tip of the T3SS needle and aids PopB and PopD in their membrane disruption process (Gébus et al., 2009; Goure et al., 2005; Guo and Galán, 2021; Matteï et al., 2011). Crystal structures of monomeric homologs of PcrV (LcrV, SipD, BipD) have shown that they fold into an elongated coiled-coil buttressed by an a-helical hairpin at the N-terminus and an α/β carboxy-terminal region (Derewenda, 2011; Erskine et al., 2006; Lunelli et al., 2011). Notably, the cryo-EM structure of a needle filament complex composed of PrgI (needle protein) with SipD (tip protein) at its extremity confirmed that the latter forms a pentamer where the first and fifth subunits

are separated by a gap, thus generating a heterogeneous assembly (Guo and Galán, 2021). This arrangement could be similar in numerous T3SS systems (Habenstein et al., 2019).

Given the importance of the T3SS for *P. aeruginosa* infection, components such as PcrV and PscF have been explored as targets for the development of therapeutic Abs and inhibitory small molecules, respectively (Berube et al., 2017; Bowlin et al., 2014). Animal models have shown that blocking the T3SS, particularly the function of PcrV, can successfully diminish tissue damage due to *P. aeruginosa* infection (Frank et al., 2002; Imamura et al., 2007). Moreover, in ventilated patients, pegylated Fabs that target PcrV (KB001-A) were shown to successfully reduce the incidence of pneumonia, which is consistent with the role of T3SS in the acute phase of infection (Jain et al., 2018; Roy-Burman et al., 2001). However, this treatment did not benefit chronically colonized CF patients in terms of antibiotic needs (François et al., 2012; Jain et al., 2018; Yaeger et al., 2021). In addition, the bispecific MEDI3902 mAb targeting both PcrV and the Psl exopolysaccharide successfully protected against *P. aeruginosa* infection in animal models but was discontinued in phase II clinical trials (Chastre et al., 2022; DiGiandomenico et al., 2014). Nevertheless, PcrV remains an attractive target, motivating the search for potentially more effective Abs (Simonis et al., 2023).

Here, we sorted specific single memory B cells from peripheral blood mononuclear cells (PBMCs) of cystic fibrosis patients to identify mAbs against PcrV and PscF with potential T3SS-inhibiting activity. Two anti-PcrV mAbs (P5B3 and P3D6) showed inhibition of the injection of the T3SS effector ExoS into epithelial cells, with mAb P5B3 displaying blocking activity against five major PcrV variants representing more than 80% of clinical isolates sequenced to date. We obtained the crystal structure of a P3D6 Fab-PcrV complex and further compared the mechanisms of actions of different anti-PcrV mAbs targeting various epitopes, including one mAb from a recent publication (Simonis et al., 2023). These structure-based analyses of the mechanisms of action of the different mAbs provide valuable insights for the development of improved antipseudomonal treatments and preventive approaches.

148 **RESULTS**

149

150 **Selection of donors exhibiting T3SS-inhibiting circulating IgG responses**

151 Our approach was based on single cell sorting of recombinant PcrV and PscF
152 specific memory B cells from human donor peripheral blood mononuclear cells
153 (PBMCs). To identify donors with anti-PcrV and -PscF mAbs with T3SS-inhibitory
154 activity, we first evaluated in ELISA the reactivity of sera from a cohort of CF patients
155 that were chronically colonized with *P. aeruginosa* against recombinant PcrV and PscF
156 before testing them in functional assays (Figure 1A). Among the 34 sera tested, donors
157 16 and 25 exhibited the strongest reactivity for both proteins (Figure 1B).

158 To assess the capacity of Protein A-purified serum IgGs (predominantly IgG1,
159 IgG2 and IgG4) to block T3SS effector translocation, we used a previously developed
160 cellular model that is based on the T3SS-dependent translocation of the ExoS effector
161 fused to β-lactamase, ExoS-Bla (Verove et al., 2012). Briefly, epithelial cells were
162 exposed to *P. aeruginosa* CHA∆*exoS* expressing the ExoS-Bla reporter in the
163 presence of patients' polyclonal purified IgGs. ExoS-Bla translocation was measured
164 by monitoring fluorescence of the β-lactamase FRET-competent substrate CCF2-AM,
165 and expressed as normalized reporter injection. Polyclonal IgGs from donors 16 and
166 25 showed a potent ExoS-Bla translocation blocking activity with an almost complete
167 inhibition of injection at 160 µg/mL (Figure 1C). To investigate whether the observed
168 activity was driven by anti-PcrV and/or anti-PscF specific IgGs, we absorbed specific
169 Abs on beads coated with recombinant PcrV or PscF to obtain polyclonal IgG samples
170 depleted of the corresponding specific IgGs (Figure 1D, top). The T3SS-blocking
171 activity of depleted polyclonal IgGs was then evaluated using the same method as
172 above (Figure 1D, bottom). The results showed a decrease in inhibitory activity when
173 anti-PcrV Abs were depleted from donor 25's IgGs and when anti-PscF Abs were
174 depleted from donor 16's IgGs, suggesting the presence of inhibitory Abs against the
175 respective proteins. Additionally, the findings demonstrated that our recombinant
176 antigen baits could effectively bind T3SS-inhibitory Abs and could therefore be used to
177 isolate memory B cells producing the corresponding IgGs.

178

179 **Isolation of PcrV and PscF mAbs using a single cell direct sorting approach**

180 To isolate mAbs specific to PcrV and PscF, PBMCs were purified from whole
181 blood from the two selected donors. Next, using single cell sorting, IgG positive
182 memory B cells were isolated based on their ability to recognize either PscF or PcrV
183 (Figure 2A) and seeded at the frequency of one cell per well. Variable heavy and light
184 chain gene sequences were retrieved from isolated B cells leading to the production of
185 a total of 66 recombinant mAbs (53 and 13 putative anti-PscF and anti-PcrV,
186 respectively). The specific binding capacities of 10 anti-PscF and 4 anti-PcrV mAbs
187 were confirmed by ELISA against the corresponding recombinant proteins. EC_{50} values
188 calculated from ELISA data showed variable apparent affinities ranging from ~50
189 µg/mL to 0.02 µg/mL (Figure 2B). Isolated mAbs originated from a variety of variable
190 gene germline families, as determined using the international immunogenetics
191 information system (IMGT) database alignments, and did not present any notable
192 features in term of mutation rates or HCDR3 length (Supplementary Table 1), with no
193 particular enrichment noted.

194 The ability of ELISA-confirmed anti-PscF and anti-PcrV mAbs to block T3SS-
195 mediated activity at a concentration of 100 µg/mL was subsequently evaluated using
196 the ExoS-Bla reporter system. No significant reduction in ExoS-Bla injection was
197 observed for any of the anti-PscF mAbs tested. However, two out of four anti-PcrV
198 mAbs, P5B3 and P3D6, significantly reduced ExoS-Bla injection, with P3D6 displaying
199 significantly stronger efficacy (Figure 2B).

200 To map the epitopes of the isolated mAbs, we next performed competition
201 ELISAs (Supplementary Table 2). Antibodies directed at PscF grouped into three
202 clusters, with P1D8 and P5G10 mAbs competing only against themselves. Similarly,
203 anti-PcrV mAbs also grouped into three clusters, with the two anti-PcrV mAbs
204 exhibiting T3SS inhibitory activity, P5B3 and P3D6, seemingly targeting overlapping
205 epitopes. Precise affinities of both mAbs were measured using biolayer interferometry
206 (BLI), revealing subnanomolar K_D values (Supplementary Table 3). Notably, P3D6
207 exhibited approximately 30-fold lower affinity compared to P5B3, despite
208 demonstrating greater efficacy in the inhibitory assay.

209

210 **P5B3 inhibits T3SS-dependent toxin injection by recognizing a highly**
211 **conserved epitope of PcrV**

212 Polymorphism in PcrV protein sequences was reported among *P. aeruginosa*
213 clinical isolates and should be considered in the development of therapeutic human
214 monoclonal Abs targeting PcrV (Figure 3A) (Tabor et al., 2018). To determine whether
215 the blocking activity of mAbs P5B3 and P3D6 was impacted by the PcrV sequence,
216 the reporter ExoS-Bla was introduced into a strain that lacked isogenic PcrV (Δ*pcrV*)
217 and synthetized the five most prevalent PcrV variants found in over 80% of clinical
218 isolates (Tabor et al., 2018). Monoclonal Ab P5B3 showed statistically significant T3SS
219 blocking activity towards all variants (Figure 3B) with estimated IC_{50} values ranging
220 from 100 µg/mL to 400 µg/mL for the five variants (no statistically significant difference;
221 Supplementary Figure 1). In contrast, mAb P3D6 had no effect on variants 2, 3, 4 and
222 5, but strongly inhibited variant 1 (Figure 3B) with an estimated IC_{50} of 3.7 µg/mL
223 (Supplementary Figure 1), indicating that the epitope recognized by P3D6 differs
224 between PcrV variants.

225

226 **Anti-PcrV mAbs block translocon pore assembly**

227 It has been suggested that PcrV scaffolds the assembly of the PopB/PopD
228 translocon within host membranes by interacting with the PopD component of the pore
229 (Goure et al., 2004; Kundracik et al., 2022, 2022; Matteï et al., 2011). Furthermore,
230 polyclonal Abs raised against PcrV have been shown to inhibit the assembly of the
231 translocon in target membranes (Goure et al., 2005).

232 To investigate the mechanistic details of the inhibitory activity of mAbs P3D6
233 and P5B3, we used a *P. aeruginosa* strain deprived of all three T3SS effectors, ExoS,
234 ExoT and ExoY. This strain, named PAO1Δ3Tox (Cisz et al., 2008) harbors PcrV
235 variant 1 and provokes toxin-independent macrophage pyroptosis upon membrane
236 insertion of the PopB/PopD translocation pore (Dacheux et al., 2001). Death of J774
237 macrophages was monitored during 4h post-infection by measuring an increase in
238 propidium iodide fluorescence due to DNA binding to the nuclei of dead cells. Both
239 mAbs significantly reduced the cytotoxicity induced by PAO1Δ3Tox by 28% and 73%,
240 respectively (Figure 4A). Monoclonal Ab P3D6 exhibited a dose-response inhibition

241 with an estimated IC_{50} of 11.8 µg/mL (Figure 4B), while P5B3 did not exhibit a
242 significant dose-response effect at concentrations below 100 µg/mL (Figure 4C).
243 Overall, these results indicate that the binding of both mAbs to PcrV reduces the
244 formation of the translocation pore in target cell membranes, with P3D6 exhibiting more
245 potent activity.

246

247 **Crystal structure of PcrV* bound to Fab P3D6**

248 In order to identify the PcrV epitopes recognized by the two mAbs, we generated
249 a plasmid encoding a form of PcrV (PcrV*) amenable to crystallization (Tabor et al.,
250 2018) as well as Fab fragments from both P3D6 and P5B3 mAbs. PcrV* was expressed
251 in *E. coli* while both Fabs were expressed in HEK293F cells. Individual proteins were
252 purified by affinity and size-exclusion chromatographies. PcrV* was incubated with
253 either Fab fragment and samples were co-purified using size exclusion
254 chromatography. Despite the fact that both PcrV*-Fab P3D6 and PcrV*-Fab P5B3
255 complexes co-eluted in gel filtration, only the PcrV*-Fab P3D6 complex subsequently
256 generated diffracting crystals. Data were collected at the ESRF synchrotron in
257 Grenoble and the structure was solved by molecular replacement using Phaser
258 (McCoy et al., 2007). Iterative manual model building and model improvement led to
259 the structure whose statistics for data collection and refinement are presented in
260 Supplementary Table 4.

261 PcrV* is composed of six helices interwoven by loop regions. α-helices 1, 4 and
262 6 are the major secondary structure elements in PcrV*, while helices 2, 3 and 5 are 1-
263 or 2-turn helices. Most of the contacts formed between PcrV* and Fab P3D6 involve
264 Helix 6 and the loop preceding it (Figures 5A, 5B) and implicate a binding platform
265 made by both LC and HC from Fab P3D6 (Supplementary figure 3). From the PcrV
266 side, the interaction region is highly polar, being formed by the side chains of Lys208,
267 Gln217, Glu220, Lys222, Ser225, Asp 226, Tyr 228, Glu231, Asn234, Thr243, Asp246
268 and Arg247. The substitution of Ser225 in PcrV variant V1 by Lys or Arg in variants V2
269 to V5 is consistent with P3D6 being inefficient on strains harboring these four variants,
270 since a residue with a bulky side chain in this position would invariably clash with the
271 loop formed by residues 52-56 of the Fab.

272 In order to understand the protective role of mAb P3D6 in the context of the PcrV
273 pentameric oligomer located at the tip of the PscF needle, we generated a model using
274 the cryo-EM structure of the SipD pentamer (Guo and Galán, 2021) and aligned our
275 co-crystal structure onto this model (Figures 5C, 5D).This analysis revealed that Fab
276 P3D6 can successfully bind to one PcrV monomer (dark red and orange in Figure 5,
277 respectively), but would be unable to bind to a pre-formed PcrV pentamer due to the
278 generation of clashes with neighboring subunits of the oligomeric form (Figure 5; the
279 structure of the Fab can be seen overlaid with that of the pentamer subunits).

280

281 **DISCUSSION**

282 We generated a panel of anti-PscF and -PcrV human mAbs through specific
283 memory B cell sorting from selected individuals. Although adsorption experiments with
284 recombinant PscF suggested the presence of anti-PscF Abs with T3SS inhibitory
285 activity in the donor from whom they were isolated, none of the isolated mAbs exhibited
286 this activity. Competition mapping showed that the anti-PscF mAbs targeted three
287 distinct regions of PscF, none of which seemingly involved in inhibitory activity. Further
288 epitope mapping would be necessary to gain deeper insight; however, in the absence
289 of a PscF structure, this remains challenging. Isolating a greater number of mAbs from
290 a selected donor with strong anti-PscF inhibitory activity would certainly increase the
291 likelihood of identifying one with T3SS-inhibiting properties.

292 Of the four anti-PcrV mAbs isolated, two exhibited T3SS inhibitory capacity.
293 Their mechanism of action could potentially involve (i) prevention of effector secretion
294 by acting as a cap for PcrV; (ii) prevention of effector translocation towards the host
295 cell by disruption of the PcrV-PopB/PopD interaction; or (iii) prevention of
296 oligomerization of PcrV itself (Gébus et al., 2009; Sawa et al., 2019). Here, we
297 measured the ability of the inhibiting anti-PcrV mAbs we isolated to block PopB/PopD
298 pore formation and toxin injection, and carried out a mechanistic and structural analysis
299 of their activity, in parallel with other mAbs targeting PcrV.

300 We set out to investigate and compare the mechanism of action of several
301 antiPcrV mAbs: P3D6 mAb and P5B3 (this work), 30-B8 (Simonis et al., 2023), as well
302 as a previously reported humanized, bivalent PcrV-Psl mAb (DiGiandomenico et al.,
303 2014). In order to do so, we produced mAb 30-B8 and subsequently purchased mAb

304 MEDI3902 from MedChem. The P3D6, P5B3, 30-B8 and MEDI3902 mAbs were
305 notably compared by employing two assays capable of detecting T3SS inhibition, each
306 with a different readout: injection of the ExoS-Bla reporter into epithelial cells and
307 cytotoxicity measurements in macrophages as a read-out for translocon assembly. In
308 addition, we performed structural analyses on three of the mAb-PcrV complexes, from
309 the viewpoints of recognition of both monomeric and pentameric forms of PcrV.

310 Both MEDI3902 and 30-B8 mAbs potently inhibited the injection of ExoS-Bla
311 into target cells, with IC_{50} values of 117 ng/mL and 21.3 ng/mL, respectively (Figure
312 6A). Monoclonal Abs isolated in this study also inhibited toxin injection, although
313 significantly less potently, with IC_{50} values of 3.65 µg/mL for P3D6, and around 100
314 µg/mL for P5B3. Monoclonal Ab MEDI3902 had previously been shown to bind to
315 different PcrV variants (Tabor et al., 2018) and here we confirmed that mAb 30-B8 was
316 similarly efficient at inhibiting toxin injection by strains carrying five different PcrV
317 variants (Simonis et al., 2023) (Supplementary Figure 2). Monoclonal Ab P5B3 was
318 also able to inhibit all variants, but only at high concentrations, while P3D6 was only
319 active against variant V1. Therefore, P5B3 appears to recognize a highly conserved
320 epitope whereas P3D6 seems to bind an overlapping epitope that includes the variable
321 Ser225, as suggested by the ELISA mapping competition and structural data, but does
322 so in a more effective manner.

323 In the macrophage cytotoxicity assay, translocon assembly was inhibited by
324 mAbs 30-B8 (IC_{50} of 45.2 ng/mL) and P3D6 (IC_{50} of 11.8 µg/mL), while P5B3 and
325 MEDI3902 did not exhibit significant dose-response inhibition. Together, these results
326 suggest that the T3SS-inhibiting activity of these anti-PcrV Abs may occur through
327 distinct mechanisms.

328 In order to understand the differences in potency and potentially in mechanisms
329 of action at a structural level, we compared the Fab-PcrV interaction regions for the
330 P3D6, 30-B8 and MEDI3902 Fabs. Monomeric PcrV is an elongated, dumbbell-shaped
331 molecule, and the chimeric form used in this study displays the same characteristics
332 (Figure 5A). Fab MEDI3902 binds to one of the extremities of monomeric PcrV,
333 extending in the longitudinal axis of the molecule (Figure 6B, top). This mode of binding
334 is distinct from that of 30-B8 and P3D6 Fabs, both of which recognize the C-terminal
335 region of PcrV (Figure 6B, middle) (Simonis et al., 2023). Therefore, the binding region

336 of 30-B8 and P3D6 does not, by itself, appear to explain the significant difference in
337 potency between the two mAbs. Moreover, a difference in affinity does not account for
338 the difference in potency either, as both mAbs bind to recombinant monomeric PcrV
339 with comparable apparent affinities of around 30 ng/mL (our data and Simonis et al.,
340 2023).

341 In order to perform this comparative analysis in the context of a PcrV oligomer,
342 we employed the model of the PcrV pentamer generated as described above, which
343 was based on the cryo-EM structure of SipD from *S. typhimurium* (Guo and Galán,
344 2021). According to this analysis, the only Fab that is able to bind to all PcrV protomers
345 in the pentamer without generating clashes with either PcrV or other Fabs is 30-B8
346 (Figure 6). In the case of MEDI3902, the Fab can bind the oligomer, but only with a 1:5
347 stoichiometry, possibility due to clashes between Fabs. Finally, P3D6 is unable to bind
348 to a pre-formed pentamer, and can only recognize a PcrV protomer in its monomeric
349 form.

350 This structural analysis suggests different potential mechanisms of action. For
351 P3D6, the inability to bind to the pentamer points towards a mechanism involving
352 inhibition of oligomerization. Indeed, the analysis shows that binding of P3D6 to a
353 single PcrV monomer prevents the association of additional PcrV protomers through
354 Fab-protomer direct clashes. A similar mechanism of action may be suggested for
355 MEDI3902, as Fab-bound PcrV protomers cannot oligomerize, in this case due to
356 clashes between the Fabs themselves (Fig. 6). However, the fact that MEDI3902 does
357 not appear to prevent translocon insertion suggests that such a mechanism is unlikely
358 for this mAb as PcrV oligomerisation is required at the tip of the needle for translocon
359 assembly. In contrast to P3D6, MEDI3902 can bind the oligomerized PcrV pentamer
360 (with a stoichiometry of one) and its mechanism of action may thus be related to this
361 ability. Our results suggest that when MEDI3902 is bound to the PcrV oligomer, the
362 formation of the pore is not efficiently blocked while toxin injection is strongly inhibited
363 (Fig. 6). Therefore, the presence of one MEDI3902 Ab molecule at the tip of the needle
364 does not appear to efficiently prevent either the secretion of the translocator proteins
365 PopB/PopD through the needle, nor the interactions between PcrV and PopB/PopD,
366 which have been described as required for pore formation (Kundracik et al., 2022).
367 However, the MEDI3902 Ab molecule seems to interfere with further interactions

368 between PcrV and the PopB/PopB complex, or with the sensing by PcrV of the host
369 cell, both of which are needed for toxin injection (Lee et al., 2010).

370 Lastly, 30-B8, which can bind the formed pentamer with a stoichiometry of five,
371 appears to be the most effective at blocking both pore formation and toxin injection.
372 The fact that the PcrV-bound 30-B8 Ab probably projects towards the cell membrane,
373 associated with its ability to bind to the PcrV pentamer at full occupancy, may result in
374 remarkable efficacy in blocking the interactions between PcrV and PopB/PopD.

375 In conclusion, here we show that patients with chronic infection with *P. aeruginosa* can
376 elicit anti-PscF and anti-PcrV mAbs that recognize different regions within these
377 proteins. Anti-PcrV Abs can act as T3SS inhibitors through different mechanisms, with
378 some exhibiting significantly greater efficacy than others. The strategy employed here,
379 involving the analysis of structural and functional data on antiT3SS mAbs should open
380 new avenues towards deciphering the mechanism of T3SS toxin translocation and
381 enable the isolation of more effective mAbs targeting a broad range of clinical strains.

382

383 **MATERIALS and METHODS**

384 **Clinical sample collection**

385 The study was approved by the French ethics committee (ID-RCB 2020A00311-
386 38) and was carried out according to the Declaration of Helsinki, Good Clinical Practice
387 (GCP) guidelines and current French regulations. Written consent for participation was
388 not required for this study. The first phase was a non-interventional study involving data
389 and samples from human participants conducted according to Reference Methodology
390 No. 004 issued by French authorities (Commission Nationale de l'Informatique et des
391 Libertés). Screening and functional assays were performed on human sera previously
392 collected at Grenoble Alpes University Hospital (France), from CF patients chronically
393 infected with *P. aeruginosa*. Participants were all informed and did not object to this
394 phase of the study. Inclusion criteria for the second phase of the study were: patients
395 with positive screening during phase one, ≥ 18 years old, ≥32 Kg, with a programmed
396 blood sampling at Grenoble Alpes University Hospital and not being opposed to the
397 second phase of the project. Whole blood was then collected using BD Vacutainer®
398 EDTA tubes (Becton Dickinson) and PBMCs were purified by density gradient

399 centrifugation using Lymphoprep (Eurobio scientific) following manufacturing
400 guidelines. Cells were then stored in liquid nitrogen until further use.
401

402 **Bacterial strains, genetic manipulations and growth conditions**

403 *P. aeruginosa* strains used in this study are listed in Supplementary Table 5.
404 Strains were cultured in LB media at 37 °C. For infection experiments, bacteria were
405 grown until the measured optical density at 600 nm (OD_{600nm}) of 1. Genes encoding
406 the most common variants of PcrV were cloned into the *Pseudomonas* replicative
407 vector derived from pUCP21 (West et al., 1994) containing the P*pcrG* promoter that
408 drives *pcrGVHpopDB* operon expression (West et al., 1994). The plasmids, kindly
409 provided by Simona Barzu (Sanofi Pasteur, Lyon), were transformed into the *P.*
410 *aeruginosa* strain CHA lacking *pcrV* (Goure et al., 2004).
411

412 **Expression and purification of full length PcrV and PcrV***

413 Expression of full-length PcrV from strain PAO1, cloned into a pET15b vector,
414 was performed in *E. coli* BL21(DE3) as previously described, with small modifications
415 (Nanao et al., 2003). Expression was induced with 1mM of Isopropyl β-D-
416 1thiogalactopyranoside (IPTG) at OD_{600} = 0.8 AU and cells were then grown overnight
417 at 20°C with shaking at 250 rpm. Cells were harvested by centrifugation and lysed by
418 passing through a French Press 3 times at 25 Kpsi in lysis Buffer (50 mM Tris pH 8,
419 200 mM NaCl, 20 mM Imidazole) supplemented with a protein inhibitor cocktail tablet
420 (Roche). The supernatant was cleared by centrifugation at 18,000 rpm and
421 subsequently loaded onto Ni-IDA resin (Macherey-Nagel). The resin was washed with
422 lysis buffer and the sample was eluted with lysis buffer supplemented with 100 mM
423 imidazole. Fractions containing the sample were pooled and applied to a size exclusion
424 chromatography column (Superdex 200 HiLoad 16/600) pre-equilibrated in SEC buffer
425 (20 mM Tris pH 8, 150 mM NaCl, 1 mM EDTA). A chimeric form of PcrV (PcrV*)
426 consisting of amino acids 1-17 fused to 136-249 whose design was inspired by the
427 construct described in Tabor et al. (2018), was employed for crystallization purposes.
428 The purification protocol was the same as above, the only difference being that 250
429 mM imidazole was employed to elute the sample from the Ni resin.

430

431 **Expression and purification of PscF**

432 Expression of PscF from strain PAO1 was performed in *E. coli* BL21(DE3) grown
433 in Terrific Broth. Expression was induced with 1 mM IPTG at OD_{600} = 0.6 AU and cells
434 were then grown for an additional 3 hours at 37 °C with shaking at 250 rpm. Cells were
435 harvested by centrifugation and lysed by passing through a French Press 3 times at 25
436 kpsi in lysis buffer (50 mM Tris pH 8, 200 mM NaCl, 20 mM Imidazole, 2 % glycerol)
437 supplemented with a protein inhibitor cocktail tablet (Roche). The supernatant was
438 cleared by centrifugation at 18,000 rpm and applied to a Ni-IDA resin (Macherey-
439 Nagel). The resin was washed with lysis buffer and the protein was eluted in the same
440 buffer supplemented with 250 mM imidazole. Fractions were then buffer exchanged in
441 an Amicon Ultra 10 kDa cutoff concentrator against a buffer exempt of imidazole (50
442 mM Tris pH 8, 200 mM NaCl, 2 % glycerol).

443

444 **ELISA assays**

445 For direct ELISAs, 96-well ELISA plates (Fisher # 11530627 Nunc Maxisorp)
446 were coated overnight at 4° C with the respective antigen diluted to 1µg/ml in PBS.
447 Plates were then washed with PBS-Tween 0.01%, and blocked for 1 h at room
448 temperature (RT) with 3% BSA in PBS. Next, sera or mAbs serially diluted in PBS-BSA
449 1 % were added and incubated for 1h at RT. Antibody binding was detected using
450 alkaline phosphatase-coupled goat anti-human IgG (Jackson Immuno #109 056 098)
451 and a para-nitrophenylphosphate substrate (Interchim #UP 664791). The enzymatic
452 reaction was read at 405 nm using a TECAN Spark 10M plate reader. Polyclonal Abs
453 raised in rabbits against PscF and PcrV (Goure et al., 2004) were used as positive
454 controls.

455 For competition ELISAs, serial dilutions of competitor mAbs were transferred
456 into antigen-coated wells. Following a 30-minute incubation, biotinylated mAbs were
457 added to the wells at their EC_{70} concentration (effective concentration for 70% binding).
458 Binding of biotinylated mAbs was detected using alkaline phosphatase-conjugated
459 streptavidin.

460

461 **Sorting of specific memory B cells**

462 Briefly, PBMCs were stained for 30 min at 4ºC in the dark, using Facs-Buffer
463 (PBS-1X 0.5 % BSA, 2mM EDTA) with Live Dead staining (Thermo L34957),
464 Antihuman CD3-Vio-Blue (Miltenyi 130-114-519), Anti-human CD20 Pe-Vio707
465 (Miltenyi 130-111-345), Anti-human CD19 Pe-Vio707 (Miltenyi 130-113-649), Anti-
466 human IgM PE (Miltenyi 130-093-075), Anti-human IgA PE (Miltenyi 130-113-476),
467 Anti-human IgD PE (Miltenyi 130-110-643), Anti-human CD27 APC (Miltenyi 130-108-
468 336), in the presence of recombinant biotinylated His-PcrV-Avitag coupled with
469 streptavidin BUV737 (BD 612775) or streptavidin Vio-515 (Miltenyi 103-107-459), and
470 recombinant biotinylated His-PscF-Avitag coupled with streptavidin BUV496 (BD
471 612961) or streptavidin BV605 (Biolegend 405229). After washing, the cells were
472 resuspended in Facs-Buffer and PscF or PcrV positive B cells were sorted and clonally
473 seeded in 96 plates containing lysis buffer using BD FACSAria Fusion cytometer (BD
474 Biosciences).

475

476 **Isolation and production of mAbs**

477 Sequences coding for variable regions of both heavy and light (κ and λ) chains
478 were isolated by reverse transcription on total mRNA followed by a multiplex nested
479 PCR using a set of primers covering the diversity of V-region diversity. V-regions family
480 was attributed after sequencing of amplicons and alignment in the IMGT database
481 (https://imgt.org). An additional round of PCR using primers specific to the identified
482 family was performed followed by the cloning of V-regions genes into corresponding
483 vectors containing IgG1H, IgGκ and IgGλ constant regions. Regarding 30-B8, the
484 sequences coding for the variable regions of heavy and light chains were synthesized
485 by Eurofins according to the sequence published by Simonis and coworkers (Simonis
486 et al., 2023). Cloning and production were performed as described above.

487
488 Monoclonal Abs were produced by transient transfection in HEK293F cells
489 (ThermoFisher scientific) and purified by affinity chromatography using a Protein A
490 Sepharose column (Sigma #ge17-1279-03). Elution was performed with 4.5 ml of
491 glycine 0.1 M (pH 2.5), followed by neutralization with 500 µl of 1 M Tris (pH 9). Purified

492 mAbs were then subjected to buffer exchange and concentration using AmiconUltra
493 centrifugal filters (Merck #36100101).
494

495 **P3D6 and P5B3 Fab production**

496 Sequences coding for Fab fragments were obtained by inserting stop codons
497 on genes corresponding to heavy chains of the mAbs by PCR using site directed
498 mutagenesis (Quickchange II, Agilent) according to manufacturer's instructions.
499 Mutated heavy and corresponding light chain genes were cloned into appropriate
500 expression plasmids for eukaryotic cell expression and were co-transfected at a 2:1
501 ration into FreeStyle 293-F cells (ThermoFisher). Fabs were purified using
502 KappaSelect affinity chromatography (Cytiva).

503

504 **Cellular tests for T3SS activity**

505 *ExoS-Bla translocation*

506 The T3SS-dependent toxin injection into epithelial A549 cells was measured
507 using the reporter system based on Bla/CCF2 enzyme/substrate combination
508 (Charpentier and Oswald, 2004) previously described for *P. aeruginosa* (Verove et
509 al., 2012). *P. aeruginosa* strain CHAΔ*exoS* carring ExoS-Bla fusion on the
510 chromosome was used to infect A549 cells at the multiplicity of infection (MOI) of 5.
511 The level of injected ExoS-β-lactamase was measured using CCF2 substrate, as
512 described previously (Verove et al., 2012). Inhibition of ExoS-Bla translocation was
513 evaluated in the presence of serial dilutions of Protein-A purified serum IgGs and
514 mAbs. Serum IgG purification was performed as described above for mAb
515 purification. All values were normalized using noninfected cells and cells infected in
516 the absence of Abs as references.
517

518 *Pore formation / propidium iodide incorporation into macrophages*

519 To assess the formation of a T3SS translocation pore, macrophages were
520 infected with a *P. aeruginosa* strain PAO1Δ3Tox devoid of three exotoxins (Cisz et al.,
521 2008). Two days before the experiment, J774 cells were seeded in a 96-well plate
522 (Greiner, 655090) at a density of 100 000 cells per well in DMEM supplemented with
523 10% FCS. The day before the experiment, the strain was grown overnight in LB

524 medium. The next day, bacteria were sub-cultured in fresh LB media until an OD_{600nm}
525 of 1 and the macrophages were washed twice with PBS before addition of 65 µL of
526 DMEM 10% FCS containing 2 µg/mL of propidium iodide. Antibodies diluted in DMEM,
527 10% FCS (25 µL) were then added followed by 10 µL of bacteria diluted in DMEM 10%
528 FCS to give a MOI of 5. Propidium iodide fluorescence was recorded in a Fluoroskan
529 fluorimeter every 10 minutes. The data of each fluorescence kinetics of the triplicates
530 were processed in R Studio to calculate the Area Under the Curve, as described before
531 (Ngo et al., 2019). This metrics was then normalized using noninfected cells and cells
532 infected in the absence of Abs as references.
533

534 **Data processing and analysis**

535 Data from independent cell experiments were pooled and analyzed with R
536 version 4.3.2 (R Core Team, 2023) by one-way ANOVA followed by paired t-test or
537 Kuskal-Wallis followed by the Dunn test with Benjamini-Hochberg p-value adjustment.
538 Dose-response fitting was performed using the drc package (Ritz & Strebig, 2016)
539 based on a three-parameters log-logistic model and IC_{50} were compared using the
540 function comParm().
541

542 **Bio-layer interferometry**

543 BLI experiments were performed on an OctetRED96e from Satorius/FortéBio
544 (former Pall/FortéBio) and were recorded with software provided by the manufacturer
545 (Data Acquisition v11.1). All protein samples were diluted in analysis buffer (1X PBS
546 pH 7.4, 0.02% Tween-20). 10 mM glycine pH 2.0 was used as regeneration buffer.
547 Commercial SA or SAX (streptavidin) biosensors (Pall/FortéBio) were used to capture
548 biotinylated PcrV. Kinetic analyses were performed in black 96-well plates (Nunc F96
549 MicroWell, Thermo Fisher Scientific) at 25°C with agitation at 1000 rpm. After
550 incubation and equilibration of biosensors in analysis buffer, PcrV samples were
551 applied at a concentration of 2.5 mg/mL by dipping biosensors until reaching a
552 spectrum shift between 1.2 and 2 nm, followed by an additional equilibration step in
553 analysis buffer. For association measurements, all analyte samples were diluted in
554 analysis buffer at concentrations either between 3.12 and 200 nM for IgGs or between
555 50 and 3200 nM for Fab fragments. Association phases were monitored while dipping
556 the functionalized biosensors in analyte solutions for 5 min after recording a baseline

557 for 2 min, and the dissociation phases monitored in analysis buffer for 10 min. To
558 assess and monitor unspecific binding of analytes, measurements were performed with
559 biosensors treated with the same protocols but replacing ligand solutions with analysis
560 buffer. All measurements were performed in duplicate using sample preparations.
561 Kinetic data were processed with software provided by the manufacturer (Data analysis
562 HT v11.1). Signals from zero-concentration samples were subtracted from the signals
563 obtained for each functionalized biosensor and each analyte concentration. Resulting
564 specific kinetics signals were then fitted using a global fit method and 1:2 bivalent
565 analyte model for full Abs/IgG and 1:1 Langmuir model for Fab. Reported kinetics
566 parameter values were obtained by averaging the values obtained with duplicated
567 assays and reported errors as the standard deviation.
568

569 **Crystallization of the PcrV*-Fab P3D6 complex**

570 PcrV* and Fab P3D6 were mixed in a 1:2 ratio for 1 hr at room temperature prior
571 to being subjected to size exclusion chromatography using a Superdex 200 10/300GL
572 increase column in SEC buffer (20 mM Tris pH 7.4, 150 mM NaCl, 1 mM EDTA). Peaks
573 harboring PcrV*:Fab complexes in SDS-PAGE were pooled, concentrated and used
574 for crystallization trials using the ISBG HTX crystallization platform in Grenoble. Initial
575 crystallization conditions (25 % PEG 1000, 1mM $ZnCl_2$, 100 mM sodium acetate pH
576 5.5) were optimized manually, and diffracting crystals were obtained using
577 microseeding. All crystals were grown using the hanging drop vapor diffusion method
578 at 20 °C. Single crystals were mounted in cryo-loops and flash cooled in liquid nitrogen.
579 X-ray diffraction data were collected under a nitrogen stream at 100° K at the European
580 Synchrotron Radiation Facility (ESRF, Grenoble, France).

581

582 **Structure determination and refinement**

583 The best diffraction data were collected to 2.56 Å on beamline ID30A-1 (ESRF)
584 (Bowler, 2015). The diffracting crystal was in space group $P2_1$ and displayed one 1:1
585 PcrV:Fab complex per asymmetric unit. Statistics on data collection and refinement are
586 summarized in supplementary table 5. X-ray diffraction images were indexed and
587 scaled with XDS (Kabsch 2010). ADXV (Arvai, 2020) and XDSGUI (Brehm et al., 2023)
588 were used to perform data quality and resolution cutoff check-ups (Karplus and

589 Diederichs, 2015). The maximum possible resolution was determined using the
590 STARANISO server (Tickle, 2007). The reduced X-ray diffraction data was imported
591 into the CCP4 program suite (Agirre et al., 2023). The PcrV*-Fab P3D6 structure was
592 solved by molecular replacement using PHASER (McCoy et al., 2007) and an
593 AlphaFold2 ColabFold-generated model (Mirdita et al., 2022). The PcrV* and Fab
594 model chains were placed sequentially. The structure was completed by cycles of
595 manual model building with COOT (Emsley and Cowtan, 2004, p. 200). Water
596 molecules were added to the residual electron density map as implemented in COOT.
597 Crystallographic macromolecular refinement was performed with REFMAC
598 (Murshudov et al., 2011). Cycles of model building and refinement were performed until
599 R_{work} and R_{free} converged. The TLS definition was determined and validated using the
600 TLSMD (Painter and Merritt, 2006) and PARVATI (Zucker et al., 2010) servers. The
601 stereochemical quality of the refined models was verified with MOLPROBITY (Chen et
602 al., 2010, PROCHECK (Laskowski et al., 1993) and PDB-REDO (Joosten et al., 2014).
603 Secondary structure assignment was performed by DSSP (Kabsch and Sander, 1983)
604 and STRIDE (Heinig and Frishman, 2004). Figures displaying protein structures were
605 generated with PYMOL (http://www.pymol.org).

606

607

608 **ACKNOWLEDGEMENTS**

609 This work was supported by a grant from the Agence Nationale de la Recherche
610 (ANR-22-CE18-0009) to PP, AD and IA, as well as grant 183360 from the Région
611 Auvergne Rhône-Alpes to PP and AD. This work used the platforms of the Grenoble
612 Instruct-ERIC center (ISBG; UAR 3518 CNRSCEA-UGA-EMBL) within the Grenoble
613 Partnership for Structural Biology (PSB), supported by FRISBI (ANR-10-INBS-0005)
614 and GRAL, financed within the University Grenoble Alpes graduate school (Ecoles
615 Universitaires de Recherche) CBH-EUR-GS (ANR-17-EURE-0003). The IBS
616 acknowledges integration into the Interdisciplinary Research Institute of Grenoble
617 (CEA).

618 **DATA AVAILABILITY**

619 All data generated or analyzed during this study are included in the manuscript
620 and supporting files, with the exception of the final refined model coordinates and

621 structure factors corresponding to the PcrV*- Fab P3D6 complex. Those were
622 deposited in the Protein Data Bank (PDB, https://www.rcsb.org), ID code: 9FM0.

623 **REFERENCES**

624 Agirre J, Atanasova M, Bagdonas H, Ballard CB, Baslé A, Beilsten-Edmands J, Borges
625 RJ, Brown DG, Burgos-Mármol JJ, Berrisford JM, Bond PS, Caballero I, Catapano L,
626 Chojnowski G, Cook AG, Cowtan KD, Croll TI, Debreczeni JÉ, Devenish NE, Dodson
627 EJ, Drevon TR, Emsley P, Evans G, Evans PR, Fando M, Foadi J, Fuentes-Montero
628 L, Garman EF, Gerstel M, Gildea RJ, Hatti K, Hekkelman ML, Heuser P, Hoh SW,
629 Hough MA, Jenkins HT, Jiménez E, Joosten RP, Keegan RM, Keep N, Krissinel EB,
630 Kolenko P, Kovalevskiy O, Lamzin VS, Lawson DM, Lebedev AA, Leslie AGW,
631 Lohkamp B, Long F, Malý M, McCoy AJ, McNicholas SJ, Medina A, Millán C, Murray
632 JW, Murshudov GN, Nicholls RA, Noble MEM, Oeffner R, Pannu NS, Parkhurst JM,
633 Pearce N, Pereira J, Perrakis A, Powell HR, Read RJ, Rigden DJ, Rochira W, Sammito
634 M, Sánchez Rodríguez F, Sheldrick GM, Shelley KL, Simkovic F, Simpkin AJ, Skubak
635 P, Sobolev E, Steiner RA, Stevenson K, Tews I, Thomas JMH, Thorn A, Valls JT, Uski
636 V, Usón I, Vagin A, Velankar S, Vollmar M, Walden H, Waterman D, Wilson KS, Winn
637 MD, Winter G, Wojdyr M, Yamashita K. 2023. The *CCP* 4 suite: integrative software
638 for macromolecular crystallography. *Acta Crystallogr D Struct Biol* **79**:449–461.
639 doi:10.1107/S2059798323003595

640 Arvai, A. (2020). ADXV. A Program to Display X-ray Diffraction Images.
641 https://www.scripps.edu/tainer/arvai/adxv.html. n.d.

642 Berube BJ, Murphy KR, Torhan MC, Bowlin NO, Williams JD, Bowlin TL, Moir DT,
643 Hauser AR. 2017. Impact of Type III Secretion Effectors and of Phenoxyacetamide
644 Inhibitors of Type III Secretion on Abscess Formation in a Mouse Model of
645 Pseudomonas aeruginosa Infection. *Antimicrob Agents Chemother* **61**:e01202-17.
646 doi:10.1128/AAC.01202-17

647 Bowlin NO, Williams JD, Knoten CA, Torhan MC, Tashjian TF, Li B, Aiello D, Mecsas
648 J, Hauser AR, Peet NP, Bowlin TL, Moir DT. 2014. Mutations in the Pseudomonas
649 aeruginosa Needle Protein Gene *pscF* Confer Resistance to Phenoxyacetamide
650 Inhibitors of the Type III Secretion System. *Antimicrob Agents Chemother* **58**:2211–
651 2220. doi:10.1128/AAC.02795-13

652 Brehm W, Triviño J, Krahn JM, Usón I, Diederichs K. 2023. *XDSGUI* : a graphical user
653 interface for *XDS* , *SHELX* and *ARCIMBOLDO*. *J Appl Crystallogr* **56**:1585–1594.
654 doi:10.1107/S1600576723007057

655 Charpentier X, Oswald E. 2004. Identification of the Secretion and Translocation
656 Domain of the Enteropathogenic and Enterohemorrhagic *Escherichia coli* Effector Cif,
657 Using TEM-1 β-Lactamase as a New Fluorescence-Based Reporter. *J Bacteriol*
658 **186**:5486–5495. doi:10.1128/JB.186.16.5486-5495.2004

659 Chastre J, François B, Bourgeois M, Komnos A, Ferrer R, Rahav G, De Schryver N,
660 Lepape A, Koksal I, Luyt C-E, Sánchez-García M, Torres A, Eggimann P, Koulenti D,
661 Holland TL, Ali O, Shoemaker K, Ren P, Sauser J, Ruzin A, Tabor DE, Akhgar A, Wu

662 Y, Jiang Y, DiGiandomenico A, Colbert S, Vandamme D, Coenjaerts F, MalhotraKumar
663 S, Timbermont L, Oliver A, Barraud O, Bellamy T, Bonten M, Goossens H, Reisner C,
664 Esser MT, Jafri HS, The COMBACTE-MAGNET EVADE Study Group, Joannidis M,
665 Klimscha W, De Waele E, Devriendt J, Huberlant V, Depuydt P, Van Boxstael S, Peric
666 M, Kopic J, Hanauer M, Hruby T, Sramek V, Svoboda P, Vymazal T, Novacek M,
667 Annane D, Mira J-P, Souweine B, Dequin P-F, Meziani F, Stephan F, Nseir S, Gibot
668 S, Schwebel C, Plantefeve G, Diehl J-L, Richard C, Lamer C, Klouche K, Jaber S,
669 Zakynthinos E, Filntisis G, Zakynthinos S, Koutsoukou A, Saroglou G, Nikolaou C,
670 Vlachogianni G, Pnevmatikos I, Mandragos K, Kremer I, Rozgonyi ZD, Marjanek Z,
671 Martin-Loeches I, Singer P, Van Heerden V, Carmeli Y, Povoa P, Seoane AA, Moura
672 P, Gonzalez F, Ramirez P, Marti AT, Roca RF, Oteiza L, Escudero D, Piacentini E,
673 Vera P, Tamayo L, Gallego MAG, Canas BS, Figueira I, Leon R, Korten V, Akova M,
674 Wyncoll D, Whitehouse T, Hopkins P, Sim M, Golan Y, Zervos M, Vazquez J,
675 Cherabuddi K, Smulian G, Rouphael N, Welker J, Sims M, Van Duin D, McCarthy T,
676 Polk C. 2022. Safety, efficacy, and pharmacokinetics of gremubamab (MEDI3902), an
677 anti-Pseudomonas aeruginosa bispecific human monoclonal antibody, in P.
678 aeruginosa-colonised, mechanically ventilated intensive care unit patients: a
679 randomised controlled trial. *Crit Care* **26**:355. doi:10.1186/s13054-022-04204-9

680 Chen VB, Arendall WB, Headd JJ, Keedy DA, Immormino RM, Kapral GJ, Murray LW,
681 Richardson JS, Richardson DC. 2010. *MolProbity*: all-atom structure validation for
682 macromolecular crystallography. *Acta Crystallogr D Biol Crystallogr* **66**:12–21.
683 doi:10.1107/S0907444909042073

684 Cisz M, Lee P-C, Rietsch A. 2008. ExoS Controls the Cell Contact-Mediated Switch to
685 Effector Secretion in *Pseudomonas aeruginosa*. *J Bacteriol* **190**:2726–2738.
686 doi:10.1128/JB.01553-07

687 Coburn B, Sekirov I, Finlay BB. 2007. Type III Secretion Systems and Disease. *Clin*
688 *Microbiol Rev* **20**:535–549. doi:10.1128/CMR.00013-07

689 Crowe JE. 2022. Human Antibodies for Viral Infections. *Annu Rev Immunol* **40**:349–
690 386. doi:10.1146/annurev-immunol-042718-041309

691 Dacheux D, Goure J, Chabert J, Usson Y, Attree I. 2001. Pore-forming activity of type
692 III system-secreted proteins leads to oncosis of *Pseudomonas aeruginosa* -infected
693 macrophages. *Molecular Microbiology* **40**:76–85.
694 doi:10.1046/j.13652958.2001.02368.x

695 De Melo AG, Morency C, Moineau S. 2024. Virulence-associated factors as targets for
696 phage infection. *Current Opinion in Microbiology* **79**:102471.
697 doi:10.1016/j.mib.2024.102471

698 Derewenda ZS. 2011. It's all in the crystals…. *Acta Crystallogr D Biol Crystallogr*
699 **67**:243–248. doi:10.1107/S0907444911007797

700 Diepold A, Wagner S. 2014. Assembly of the bacterial type III secretion machinery.
701 *FEMS Microbiol Rev* **38**:802–822. doi:10.1111/1574-6976.12061

702 DiGiandomenico A, Keller AE, Gao Cuihua, Rainey GJ, Warrener P, Camara MM,
703 Bonnell J, Fleming R, Bezabeh B, Dimasi N, Sellman BR, Hilliard J, Guenther CM,
704 Datta V, Zhao W, Gao Changshou, Yu X-Q, Suzich JA, Stover CK. 2014. A
705 multifunctional bispecific antibody protects against *Pseudomonas aeruginosa*. *Sci*
706 *Transl Med* **6**. doi:10.1126/scitranslmed.3009655

707 Dortet L, Lombardi C, Cretin F, Dessen A, Filloux A. 2018. Pore-forming activity of the
708 Pseudomonas aeruginosa type III secretion system translocon alters the host
709 epigenome. *Nat Microbiol* **3**:378–386. doi:10.1038/s41564-018-0109-7

710 Duan L, Zhang J, Chen Z, Gou Q, Xiong Q, Yuan Y, Jing H, Zhu J, Ni L, Zheng Y, Liu
711 Z, Zhang X, Zeng H, Zou Q, Zhao Z. 2021. Antibiotic Combined with Epitope-Specific
712 Monoclonal Antibody Cocktail Protects Mice Against Bacteremia and Acute
713 Pneumonia from Methicillin-Resistant Staphylococcus aureus Infection. *JIR* **Volume**
714 **14**:4267–4282. doi:10.2147/JIR.S325286

715 Emsley P, Cowtan K. 2004. *Coot* : model-building tools for molecular graphics. *Acta*
716 *Crystallogr D Biol Crystallogr* **60**:2126–2132. doi:10.1107/S0907444904019158

717 Erskine PT, Knight MJ, Ruaux A, Mikolajek H, Sang NWF, Withers J, Gill R, Wood SP,
718 Wood M, Fox GC, Cooper JB. 2006. High Resolution Structure of BipD: An Invasion
719 Protein Associated with the Type III Secretion System of Burkholderia Pseudomallei.
720 *Journal of Molecular Biology* **363**:125–136. doi:10.1016/j.jmb.2006.07.069

721 Faudry E, Vernier G, Neumann E, Forge V, Attree I. 2006. Synergistic Pore Formation
722 by Type III Toxin Translocators of *Pseudomonas aeruginosa*. *Biochemistry* **45**:8117–
723 8123. doi:10.1021/bi060452+

724 François B, Luyt C-E, Dugard A, Wolff M, Diehl J-L, Jaber S, Forel J-M, Garot D, Kipnis
725 E, Mebazaa A, Misset B, Andremont A, Ploy M-C, Jacobs A, Yarranton G, Pearce T,
726 Fagon J-Y, Chastre J. 2012. Safety and pharmacokinetics of an anti-PcrV PEGylated
727 monoclonal antibody fragment in mechanically ventilated patients colonized with
728 Pseudomonas aeruginosa: A randomized,double-blind, placebo-controlled trial*.
729 *Critical Care Medicine* **40**:2320–2326. doi:10.1097/CCM.0b013e31825334f6

730 Frank DW, Vallis A, Wiener-Kronish JP, Roy-Burman A, Spack EG, Mullaney BP,
731 Megdoud M, Marks JD, Fritz R, Sawa T. 2002. Generation and Characterization of a
732 Protective Monoclonal Antibody to *Pseudomonas aeruginosa* PcrV. *J INFECT DIS*
733 **186**:64–73. doi:10.1086/341069

734 Gébus C, Faudry E, Bohn Y-ST, Elsen S, Attree I. 2009. Oligomerization of PcrV and
735 LcrV, protective antigens of Pseudomonas aeruginosa and Yersinia pestis. *Journal of*
736 *Biological Chemistry* **284**:21776. doi:10.1074/jbc.A803146200

737 Goure J, Broz P, Attree O, Cornelis GR, Attree I. 2005. Protective Anti-V Antibodies
738 Inhibit *Pseudomonas* and *Yersinia* Translocon Assembly within Host Membranes. *J*
739 *INFECT DIS* **192**:218–225. doi:10.1086/430932

740 Goure J, Pastor A, Faudry E, Chabert J, Dessen A, Attree I. 2004. The V Antigen of
741 *Pseudomonas aeruginosa* Is Required for Assembly of the Functional PopB/PopD
742 Translocation Pore in Host Cell Membranes. *Infect Immun* **72**:4741–4750.
743 doi:10.1128/IAI.72.8.4741-4750.2004

744 Guo EZ, Galán JE. 2021. Cryo-EM structure of the needle filament tip complex of the
745 *Salmonella* type III secretion injectisome. *Proc Natl Acad Sci USA* **118**:e2114552118.
746 doi:10.1073/pnas.2114552118

747 Habenstein B, El Mammeri N, Tolchard J, Lamon G, Tawani A, Berbon M, Loquet A.
748 2019. Structures of Type III Secretion System Needle Filaments In: Wagner S, Galan
749 JE, editors. Bacterial Type III Protein Secretion Systems, Current Topics in
750 Microbiology and Immunology. Cham: Springer International Publishing. pp. 109–131.
751 doi:10.1007/82_2019_192

752 Hauser AR. 2009. The type III secretion system of Pseudomonas aeruginosa: infection
753 by injection. *Nat Rev Microbiol* **7**:654–665. doi:10.1038/nrmicro2199

754 Heinig M, Frishman D. 2004. STRIDE: a web server for secondary structure
755 assignment from known atomic coordinates of proteins. *Nucleic Acids Research*
756 **32**:W500–W502. doi:10.1093/nar/gkh429

757 Horcajada JP, Montero M, Oliver A, Sorlí L, Luque S, Gómez-Zorrilla S, Benito N, Grau
758 S. 2019. Epidemiology and Treatment of Multidrug-Resistant and Extensively
759 DrugResistant Pseudomonas aeruginosa Infections. *Clin Microbiol Rev* **32**:e00031-19.
760 doi:10.1128/CMR.00031-19

761 Hu Y, Huang H, Cheng X, Shu X, White AP, Stavrinides J, Köster W, Zhu G, Zhao Z,
762 Wang Y. 2017. A global survey of bacterial type III secretion systems and their
763 effectors. *Environmental Microbiology* **19**:3879–3895. doi:10.1111/1462-2920.13755

764 Imamura Y, Yanagihara K, Fukuda Y, Kaneko Y, Seki M, Izumikawa K, Miyazaki Y,
765 Hirakata Y, Sawa T, Wiener-Kronish JP, Kohno S. 2007. Effect of anti-PcrV antibody
766 in a murine chronic airway Pseudomonas aeruginosa infection model. *European*
767 *Respiratory Journal* **29**:965–968. doi:10.1183/09031936.00147406

768 Jain R, Beckett VV, Konstan MW, Accurso FJ, Burns JL, Mayer-Hamblett N, Milla C,
769 VanDevanter DR, Chmiel JF. 2018. KB001-A, a novel anti-inflammatory, found to be
770 safe and well-tolerated in cystic fibrosis patients infected with Pseudomonas
771 aeruginosa. *Journal of Cystic Fibrosis* **17**:484–491. doi:10.1016/j.jcf.2017.12.006

772 Joosten RP, Long F, Murshudov GN, Perrakis A. 2014. The *PDB_REDO* server for
773 macromolecular structure model optimization. *IUCrJ* **1**:213–220.
774 doi:10.1107/S2052252514009324

775 Kabsch W, Sander C. 1983. Dictionary of protein secondary structure: Pattern
776 recognition of hydrogen-bonded and geometrical features. *Biopolymers* **22**:2577–
777 2637. doi:10.1002/bip.360221211

778 Karplus PA, Diederichs K. 2015. Assessing and maximizing data quality in
779 macromolecular crystallography. *Current Opinion in Structural Biology* **34**:60–68.
780 doi:10.1016/j.sbi.2015.07.003

781 Kaufmann SHE, Dorhoi A, Hotchkiss RS, Bartenschlager R. 2018. Host-directed
782 therapies for bacterial and viral infections. *Nat Rev Drug Discov* **17**:35–56.
783 doi:10.1038/nrd.2017.162

784 Kundracik E, Trichka J, Díaz Aponte J, Roistacher A, Rietsch A. 2022. PopB-PcrV
785 Interactions Are Essential for Pore Formation in the Pseudomonas aeruginosa Type III
786 Secretion System Translocon. *mBio* **13**:e02381-22. doi:10.1128/mbio.02381-22

787 La Guidara C, Adamo R, Sala C, Micoli F. 2024. Vaccines and Monoclonal Antibodies
788 as Alternative Strategies to Antibiotics to Fight Antimicrobial Resistance. *IJMS*
789 **25**:5487. doi:10.3390/ijms25105487

790 Laskowski RA, MacArthur MW, Moss DS, Thornton JM. 1993. PROCHECK: a program
791 to check the stereochemical quality of protein structures. *J Appl Crystallogr* **26**:283–
792 291. doi:10.1107/S0021889892009944

793 Lee P, Stopford CM, Svenson AG, Rietsch A. 2010. Control of effector export by the
794 *Pseudomonas aeruginosa* type III secretion proteins PcrG and PcrV. *Molecular*
795 *Microbiology* **75**:924–941. doi:10.1111/j.1365-2958.2009.07027.x

796 Levin MJ, Ustianowski A, De Wit S, Launay O, Avila M, Templeton A, Yuan Y,
797 Seegobin S, Ellery A, Levinson DJ, Ambery P, Arends RH, Beavon R, Dey K, Garbes
798 P, Kelly EJ, Koh GCKW, Near KA, Padilla KW, Psachoulia K, Sharbaugh A, Streicher
799 K, Pangalos MN, Esser MT. 2022. Intramuscular AZD7442 (Tixagevimab–
800 Cilgavimab) for Prevention of Covid-19. *N Engl J Med*
801 **386**:2188–2200. doi:10.1056/NEJMoa2116620

802 Lunelli M, Hurwitz R, Lambers J, Kolbe M. 2011. Crystal Structure of PrgI-SipD:
803 Insight into a Secretion Competent State of the Type Three Secretion System Needle
804 Tip and its Interaction with Host Ligands. *PLoS Pathog*
805 **7**:e1002163. doi:10.1371/journal.ppat.1002163

806 Matteï P, Faudry E, Job V, Izoré T, Attree I, Dessen A. 2011. Membrane targeting and
807 pore formation by the type III secretion system translocon. *The FEBS Journal* **278**:414–
808 426. doi:10.1111/j.1742-4658.2010.07974.x

809 McCoy AJ, Grosse-Kunstleve RW, Adams PD, Winn MD, Storoni LC, Read RJ. 2007.
810 *Phaser* crystallographic software. *J Appl Crystallogr* **40**:658–674.
811 doi:10.1107/S0021889807021206

812 Mirdita M, Schütze K, Moriwaki Y, Heo L, Ovchinnikov S, Steinegger M. 2022.
813 ColabFold: making protein folding accessible to all. *Nat Methods* **19**:679–682.
814 doi:10.1038/s41592-022-01488-1

815 Montagner C, Arquint C, Cornelis GR. 2011. Translocators YopB and YopD from
816 Yersinia enterocolitica Form a Multimeric Integral Membrane Complex in Eukaryotic
817 Cell Membranes. *J Bacteriol* **193**:6923–6928. doi:10.1128/JB.05555-11

818 Morrison C. 2015. Antibacterial antibodies gain traction. *Nat Rev Drug Discov* **14**:737–
819 738. doi:10.1038/nrd4770

820 Mueller CA, Broz P, Cornelis GR. 2008. The type III secretion system tip complex and
821 translocon. *Molecular Microbiology* **68**:1085–1095.
822 doi:10.1111/j.13652958.2008.06237.x

823 Mulangu S, Dodd LE, Davey RT, Tshiani Mbaya O, Proschan M, Mukadi D,
824 Lusakibanza Manzo M, Nzolo D, Tshomba Oloma A, Ibanda A, Ali R, Coulibaly S,
825 Levine AC, Grais R, Diaz J, Lane HC, Muyembe-Tamfum J-J. 2019. A Randomized,
826 Controlled Trial of Ebola Virus Disease Therapeutics. *N Engl J Med* **381**:2293–2303.
827 doi:10.1056/NEJMoa1910993

828 Murray CJL, Ikuta KS, Sharara F, Swetschinski L, Robles Aguilar G, Gray A, Han C,
829 Bisignano C, Rao P, Wool E, Johnson SC, Browne AJ, Chipeta MG, Fell F, Hackett S,
830 Haines-Woodhouse G, Kashef Hamadani BH, Kumaran EAP, McManigal B,
831 Achalapong S, Agarwal R, Akech S, Albertson S, Amuasi J, Andrews J, Aravkin A,
832 Ashley E, Babin F-X, Bailey F, Baker S, Basnyat B, Bekker A, Bender R, Berkley JA,
833 Bethou A, Bielicki J, Boonkasidecha S, Bukosia J, Carvalheiro C, Castañeda-Orjuela
834 C, Chansamouth V, Chaurasia S, Chiurchiù S, Chowdhury F, Clotaire Donatien R,
835 Cook AJ, Cooper B, Cressey TR, Criollo-Mora E, Cunningham M, Darboe S, Day NPJ,
836 De Luca M, Dokova K, Dramowski A, Dunachie SJ, Duong Bich T, Eckmanns T, Eibach
837 D, Emami A, Feasey N, Fisher-Pearson N, Forrest K, Garcia C, Garrett D, Gastmeier
838 P, Giref AZ, Greer RC, Gupta V, Haller S, Haselbeck A, Hay SI, Holm M, Hopkins S,
839 Hsia Y, Iregbu KC, Jacobs J, Jarovsky D, Javanmardi F, Jenney AWJ, Khorana M,
840 Khusuwan S, Kissoon N, Kobeissi E, Kostyanev T, Krapp F, Krumkamp R, Kumar A,
841 Kyu HH, Lim C, Lim K, Limmathurotsakul D, Loftus MJ, Lunn M, Ma J, Manoharan A,
842 Marks F, May J, Mayxay M, Mturi N, Munera-Huertas T, Musicha P, Musila LA,
843 MussiPinhata MM, Naidu RN, Nakamura T, Nanavati R, Nangia S, Newton P, Ngoun
844 C, Novotney A, Nwakanma D, Obiero CW, Ochoa TJ, Olivas-Martinez A, Olliaro P,

845 Ooko E, Ortiz-Brizuela E, Ounchanum P, Pak GD, Paredes JL, Peleg AY, Perrone C,
846 Phe T, Phommasone K, Plakkal N, Ponce-de-Leon A, Raad M, Ramdin T, Rattanavong
847 S, Riddell A, Roberts T, Robotham JV, Roca A, Rosenthal VD, Rudd KE, Russell N,
848 Sader HS, Saengchan W, Schnall J, Scott JAG, Seekaew S, Sharland M,
849 Shivamallappa M, Sifuentes-Osornio J, Simpson AJ, Steenkeste N, Stewardson AJ,
850 Stoeva T, Tasak N, Thaiprakong A, Thwaites G, Tigoi C, Turner C, Turner P, Van
851 Doorn HR, Velaphi S, Vongpradith A, Vongsouvath M, Vu H, Walsh T, Walson JL,
852 Waner S, Wangrangsimakul T, Wannapinij P, Wozniak T, Young Sharma TEMW, Yu
853 KC, Zheng P, Sartorius B, Lopez AD, Stergachis A, Moore C, Dolecek C, Naghavi M.
854 2022. Global burden of bacterial antimicrobial resistance in 2019: a systematic
855 analysis. *The Lancet* **399**:629–655. doi:10.1016/S0140-6736(21)02724-0

856 Murshudov GN, Skubák P, Lebedev AA, Pannu NS, Steiner RA, Nicholls RA, Winn
857 MD, Long F, Vagin AA. 2011. *REFMAC* 5 for the refinement of macromolecular crystal
858 structures. *Acta Crystallogr D Biol Crystallogr* **67**:355–367.
859 doi:10.1107/S0907444911001314

860 Nanao M, Ricard-Blum S, Di Guilmi A, Lemaire D, Lascoux D, Chabert J, Attree I,
861 Dessen A. 2003. [No title found]. *BMC Microbiol* **3**:21. doi:10.1186/1471-2180-3-21

862 Ngo T-D, Plé S, Thomas A, Barette C, Fortuné A, Bouzidi Y, Fauvarque M-O, Pereira
863 De Freitas R, Francisco Hilário F, Attrée I, Wong Y-S, Faudry E. 2019. Chimeric
864 Protein–Protein Interface Inhibitors Allow Efficient Inhibition of Type III Secretion
865 Machinery and *Pseudomonas aeruginosa* Virulence. *ACS Infect Dis* **5**:1843–1854.
866 doi:10.1021/acsinfecdis.9b00154

867 Painter J, Merritt EA. 2006. *TLSMD* web server for the generation of multi-group TLS
868 models. *J Appl Crystallogr* **39**:109–111. doi:10.1107/S0021889805038987

869 Pennini ME, De Marco A, Pelletier M, Bonnell J, Cvitkovic R, Beltramello M, Cameroni
870 E, Bianchi S, Zatta F, Zhao W, Xiao X, Camara MM, DiGiandomenico A, Semenova E,
871 Lanzavecchia A, Warrener P, Suzich J, Wang Q, Corti D, Stover CK. 2017. Immune
872 stealth-driven O2 serotype prevalence and potential for therapeutic antibodies against
873 multidrug resistant Klebsiella pneumoniae. *Nat Commun* **8**:1991.
874 doi:10.1038/s41467017-02223-7

875 Quinaud M, Chabert J, Faudry E, Neumann E, Lemaire D, Pastor A, Elsen S, Dessen
876 A, Attree I. 2005. The PscE-PscF-PscG Complex Controls Type III Secretion Needle
877 Biogenesis in Pseudomonas aeruginosa. *Journal of Biological Chemistry* **280**:36293–
878 36300. doi:10.1074/jbc.M508089200

879 Quinaud M, Plé S, Job V, Contreras-Martel C, Simorre J-P, Attree I, Dessen A. 2007.
880 Structure of the heterotrimeric complex that regulates type III secretion needle
881 formation. *Proc Natl Acad Sci USA* **104**:7803–7808. doi:10.1073/pnas.0610098104
882 Rollenske T, Szijarto V, Lukasiewicz J, Guachalla LM, Stojkovic K, Hartl K, Stulik L,
883 Kocher S, Lasitschka F, Al-Saeedi M, Schröder-Braunstein J, Von Frankenberg M,

884 Gaebelein G, Hoffmann P, Klein S, Heeg K, Nagy E, Nagy G, Wardemann H. 2018.
885 Cross-specificity of protective human antibodies against Klebsiella pneumoniae LPS
886 O-antigen. *Nat Immunol* **19**:617–624. doi:10.1038/s41590-018-0106-2

887 Roy-Burman A, Savel RH, Racine S, Swanson BL, Revadigar NS, Fujimoto J, Sawa
888 T, Frank DW, Wiener-Kronish JP. 2001. Type III Protein Secretion Is Associated with
889 Death in Lower Respiratory and Systemic *Pseudomonas aeruginosa* Infections. *J*
890 *INFECT DIS* **183**:1767–1774. doi:10.1086/320737

891 Sawa, Kinoshita, Inoue, Ohara, Moriyama. 2019. Immunoglobulin for Treating Bacterial
892 Infections: One More Mechanism of Action. *Antibodies* **8**:52.
893 doi:10.3390/antib8040052
894

895 Schoehn G, Di Guilmi AM, Lemaire D, Attree I, Weissenhorn W, Dessen A. 2003.
896 Oligomerization of type III secretion proteins PopB and PopD precedes pore formation
897 in Pseudomonas. *EMBO J*. **22**(19):4957-67. doi:10.1093/emboj/cdg499.

898 Serapio-Palacios A, Finlay BB. 2020. Dynamics of expression, secretion and
899 translocation of type III effectors during enteropathogenic Escherichia coli infection.
900 *Current Opinion in Microbiology* **54**:67–76. doi:10.1016/j.mib.2019.12.001

901 Simonis A, Kreer C, Albus A, Rox K, Yuan B, Holzmann D, Wilms JA, Zuber S, Kottege
902 L, Winter S, Meyer M, Schmitt K, Gruell H, Theobald SJ, Hellmann A-M, Meyer C,
903 Ercanoglu MS, Cramer N, Munder A, Hallek M, Fätkenheuer G, Koch M, Seifert H,
904 Rietschel E, Marlovits TC, Van Koningsbruggen-Rietschel S, Klein F, Rybniker J. 2023.
905 Discovery of highly neutralizing human antibodies targeting Pseudomonas aeruginosa.
906 *Cell* **186**:5098-5113.e19. doi:10.1016/j.cell.2023.10.002

907 Tabor DE, Oganesyan V, Keller AE, Yu L, McLaughlin RE, Song E, Warrener P,
908 Rosenthal K, Esser M, Qi Y, Ruzin A, Stover CK, DiGiandomenico A. 2018.
909 Pseudomonas aeruginosa PcrV and Psl, the Molecular Targets of Bispecific Antibody
910 MEDI3902, Are Conserved Among Diverse Global Clinical Isolates. *The Journal of*
911 *Infectious Diseases*. doi:10.1093/infdis/jiy438

912 Tickle IJ. 2007. Experimental determination of optimal root-mean-square deviations of
913 macromolecular bond lengths and angles from their restrained ideal values. *Acta*
914 *Crystallogr D Biol Crystallogr* **63**:1274–1281. doi:10.1107/S0907444907050196

915 Vacca F, Sala C, Rappuoli R. 2022. Monoclonal Antibodies for Bacterial Pathogens:
916 Mechanisms of Action and Engineering Approaches for Enhanced Effector Functions.
917 *Biomedicines* **10**:2126. doi:10.3390/biomedicines10092126

918 Verove J, Bernarde C, Bohn Y-ST, Boulay F, Rabiet M-J, Attree I, Cretin F. 2012.
919 Injection of Pseudomonas aeruginosa Exo Toxins into Host Cells Can Be Modulated
920 by Host Factors at the Level of Translocon Assembly and/or Activity. *PLoS ONE*
921 **7**:e30488. doi:10.1371/journal.pone.0030488

922 Watson A, Li H, Ma B, Weiss R, Bendayan D, Abramovitz L, Ben-Shalom N, Mor M,
923 Pinko E, Bar Oz M, Wang Z, Du F, Lu Y, Rybniker J, Dahan R, Huang H, Barkan D,
924 Xiang Y, Javid B, Freund NT. 2021. Human antibodies targeting a Mycobacterium
925 transporter protein mediate protection against tuberculosis. *Nat Commun* **12**:602.
926 doi:10.1038/s41467-021-20930-0

927 West SEH, Schweizer HP, Dall C, Sample AK, Runyen-Janecky LJ. 1994. Construction
928 of improved Escherichia-Pseudomonas shuttle vectors derived from pUC18/19 and
929 sequence of the region required for their replication in Pseudomonas aeruginosa. *Gene*
930 **148**:81–86. doi:10.1016/0378-1119(94)90237-2

931 Yaeger LN, Coles VE, Chan DCK, Burrows LL. 2021. How to kill *Pseudomonas* —
932 emerging therapies for a challenging pathogen. *Annals of the New York Academy of*
933 *Sciences* **1496**:59–81. doi:10.1111/nyas.14596

934 Zucker F, Champ PC, Merritt EA. 2010. Validation of crystallographic models
935 containing TLS or other descriptions of anisotropy. *Acta Crystallogr D Biol Crystallogr*
936 **66**:889–900. doi:10.1107/S0907444910020421

937 **FIGURES**

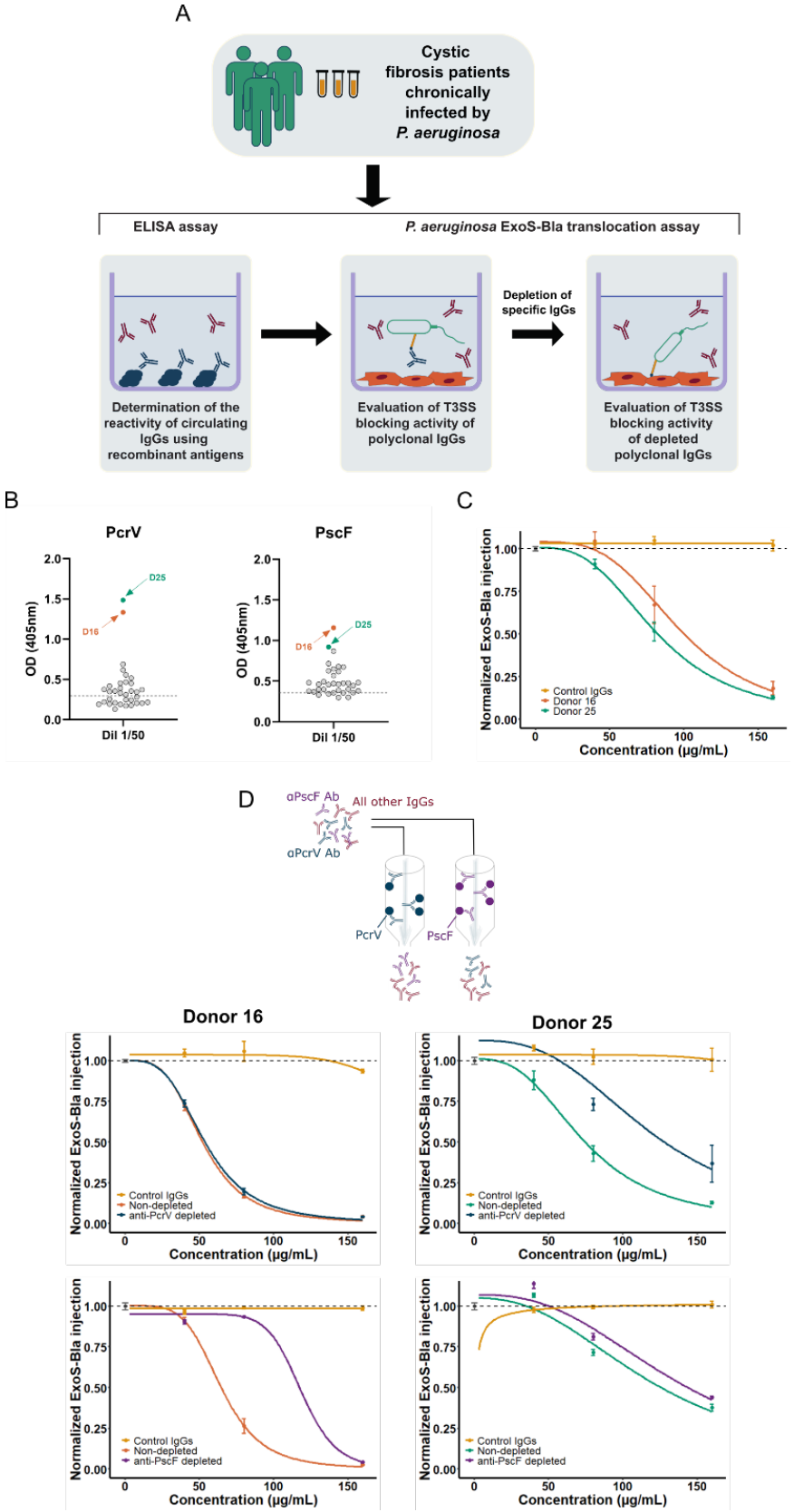

938
939

940 **Figure 1. Screening workflow and donor selection**

941 (A) Schematic representation of the workflow from patient selection to evaluation of
942 T3SS-blocking activity. (B) Patients sera (1/50 dilution) were tested in ELISA against

943 recombinant PcrV and PscF. (C) ExoS-Bla translocation blocking activity of serum
944 IgGs from donors 16 and 25. (D) (top) scheme of depletion experiment of specific Abs
945 on either PscF- or PcrV–loaded columns. (bottom) blocking activity of depleted sera
946 for both donors. The dots and bars represent the means and standard-deviations of
947 experimental triplicates. The curves correspond to the modeled log-logistic dose-
948 response curves. The dashed lines represent the mean of normalized ExoS-bla
949 injection in the absence of Ab.
950

A

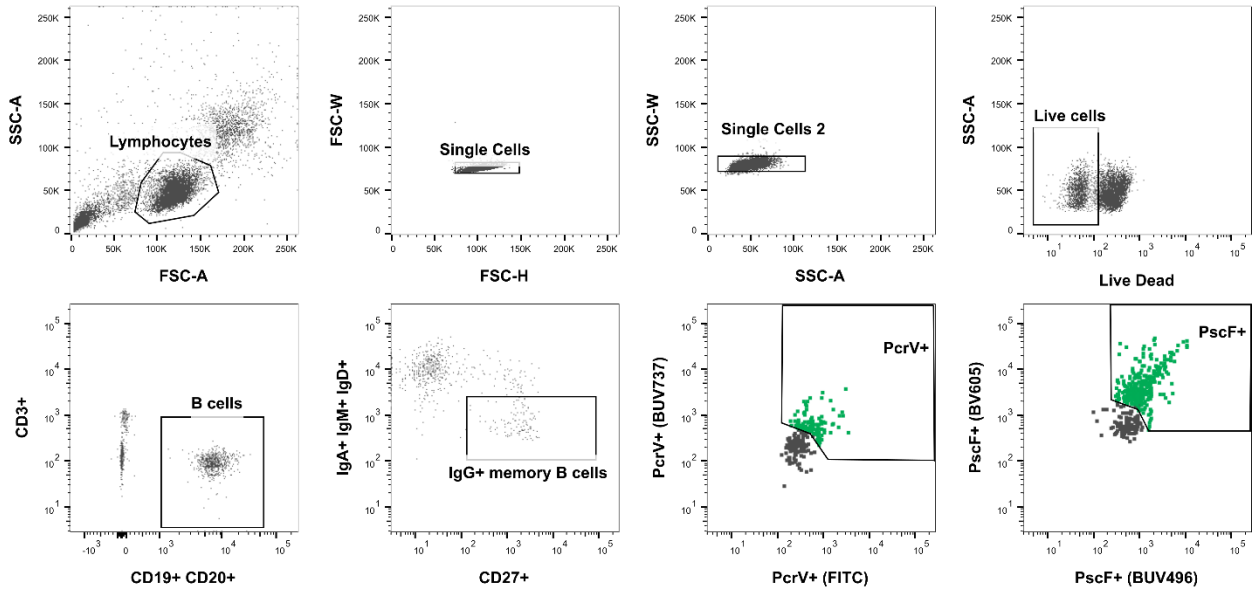

B

Anti-PcrV mAbs	EC_{50} (µg/mL)	ExoS-Bla inhibition
P5B3	0.04	24 %
P3D6	0.03	94 %
P3G9	0.08	No inhibition
P5E10	0.17	No inhibition
Anti-PscF mAbs	EC_{50} (µg/mL)	ExoS-Bla inhibition
P5G10	0.01	No inhibition
P1B7	0.07	No inhibition
P5D5	0.07	No inhibition
P1D5	0.18	No inhibition
P1B4	0.24	No inhibition
P3G6	1.28	No inhibition
P3G2	2.08	No inhibition
P1F5	4.65	No inhibition
P3G7	10.61	No inhibition
P1D7	>30	No inhibition

Figure 2. Selection of B cells from donors 16 and 25. (A) B cells sorting and isolation using PscF and PcrV baits. (B) Table summarizing the EC_{50} values of selected Abs obtained by ELISA and the percentage of inhibition of ExoS-Bla injection into epithelial cells at 100 µg/mL. ExoS-Bla inhibitions were compared using ANOVA and "No inhibition" means an absence of significant difference with the control (adjusted p-values > 0.05). The P5B3 and P3D6 mAbs exhibited differences with the control (no Ab) with adjusted p-values < 0.001.

A

Variant	Amino acid positions			
	6	9	21	225
V1 (PAO1-like)	Leu	Ala	Ser	Ser
V2 (CHA-like)	Leu	Ala	Ser	Arg
V3 (PA14-like)	Phe	Ala	Pro	Lys
V4 (PA103-like)	Phe	Gly	Pro	Arg
V5	Phe	Gly	Pro	Lys

B

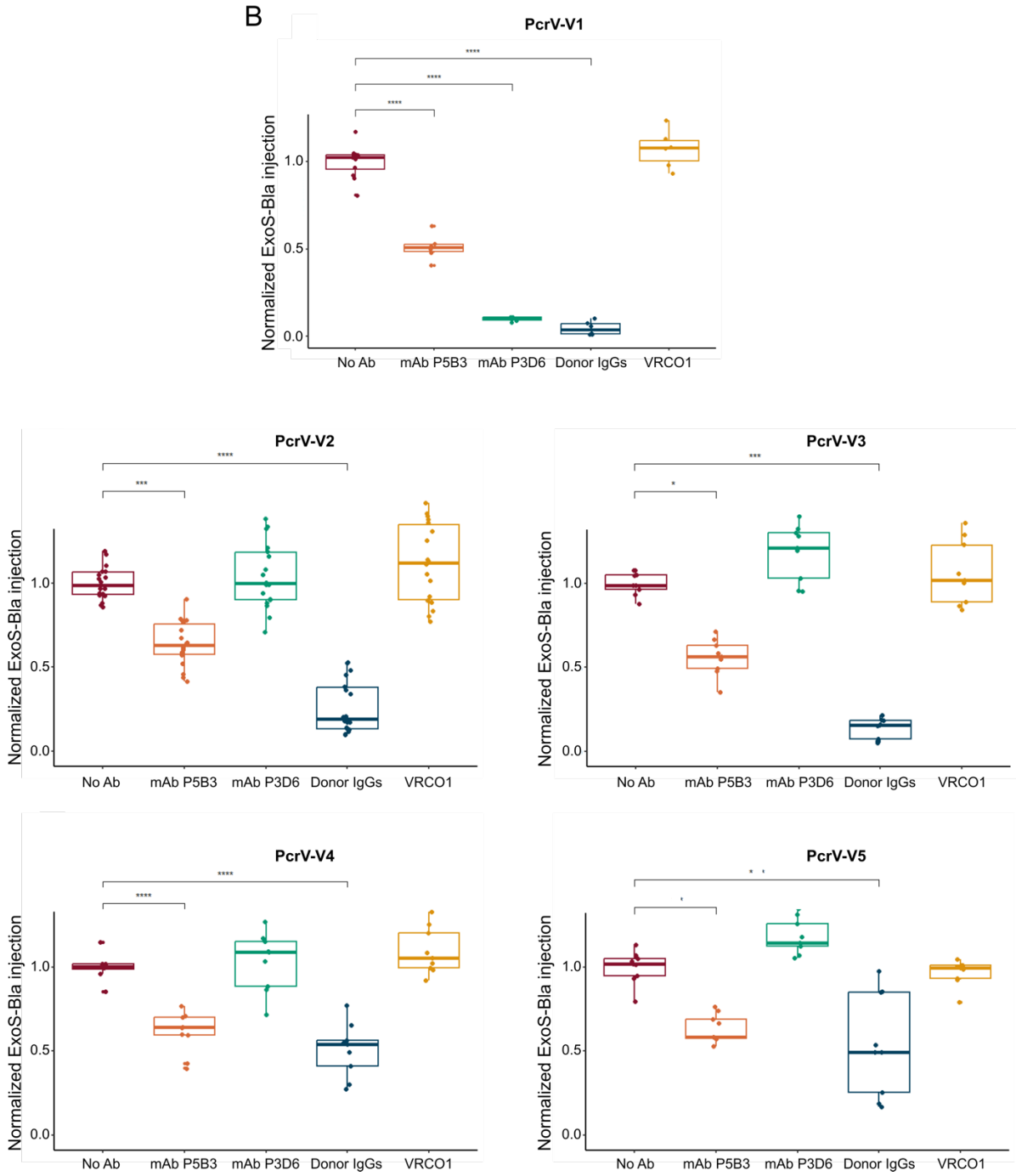

Figure 3. **mAbs P5B3 and P3D6 activity on PcrV variants**. (A) PcrV variability in clinical strains. The most variable position (225) can either be Ser, Arg or Lys. Representative strains are indicated when available (PAO1 for V1, CHA for V2, PA14

963 for V3 and PA103 for V4). (B) Inhibition of ExoS-Bla activity following infection of A549
964 epithelial cells with *P. aeruginosa* expressing the V1 variant. Normalized ExoS-Bla
965 injection values in the presence of 100 µg/mL Abs were compared to the control (no
966 Ab) using ANOVA. Pairwised t-test significance is indicated by the symbols *, **, ***
967 and **** for adjusted p-values below 0.05, 0.01, 0.001 and 0.0001, respectively. The
968 absence of symbol corresponds to adjusted p-values > 0.05.

969

970

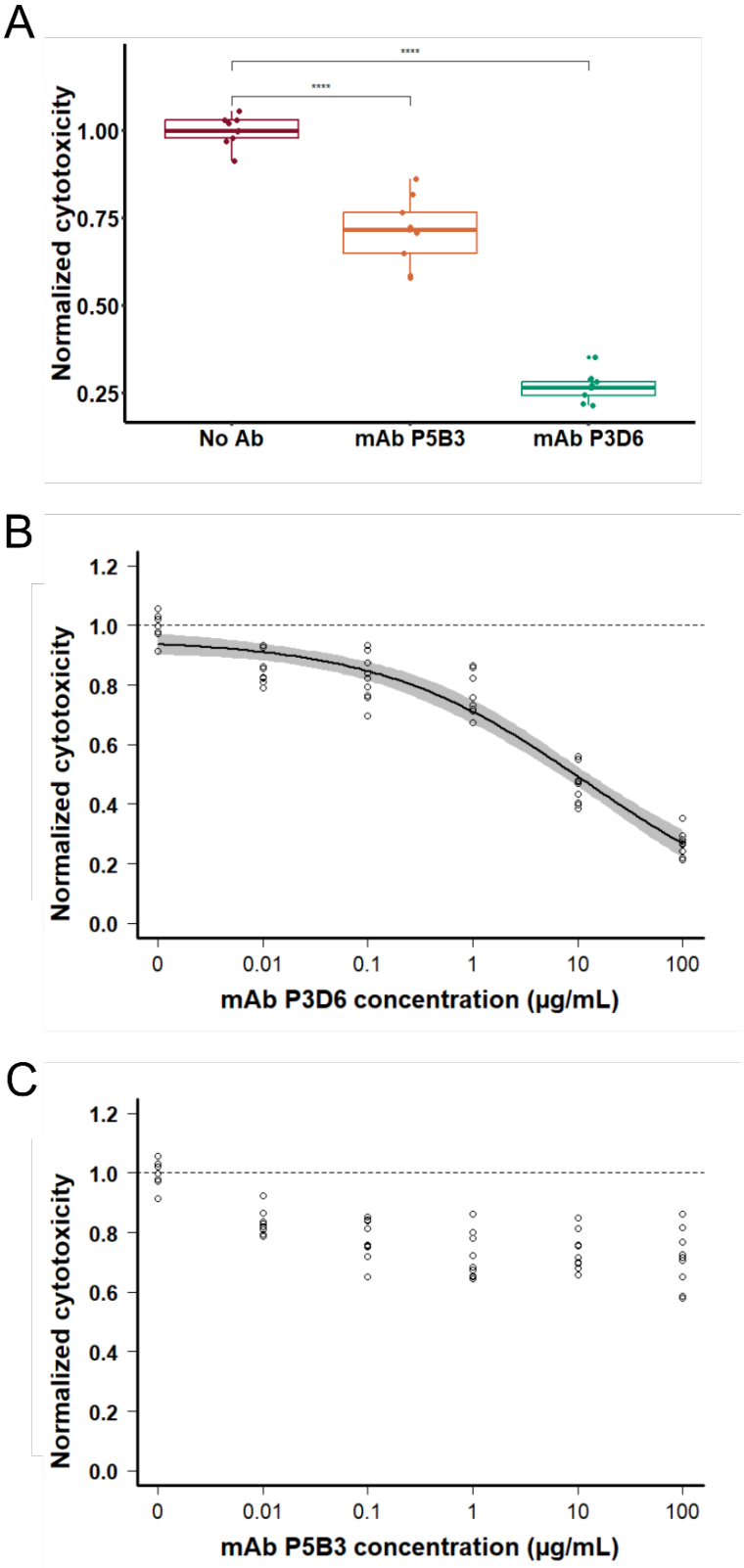

Figure 4. mAb P3D6 efficiently inhibits the PopB/PopD translocation pore. J774 macrophages were infected with *P. aeruginosa* strain (PAO1, V1) deprived of all three T3SS toxins. The cell death (cytotoxicity) resulting from insertion of the translocon pore was measured by propidium iodide incorporation and normalized to the wild-type strain

977 without addition of mAbs. (A) Normalized cytotoxicity values in the presence of mAb at
978 100 µg/mL. Specific mAbs were compared to the control (no Ab) using ANOVA.
979 Pairwised t-test significance is indicated by the symbol ****, meaning p-values below
980 0.0001. (B, C) Dose-response analysis with mAb concentrations ranging from 0.01 to
981 100 µg/mL. The circles, the black line and the grey area represent the experimental
982 values, the log-logistic modeled dose-response curve and the 95% confidence interval,
983 respectively. The dashed lines represent the mean of normalized cytotoxicity in the
984 absence of Ab.The Ab concentration is presented in logarithmic scale. No black curve
985 nor grey area is displayed for P5B3 because no dose-response could be modeled. In
986 contrast, P3D6 exhibits an IC_{50} of 11.8 µg/mL.

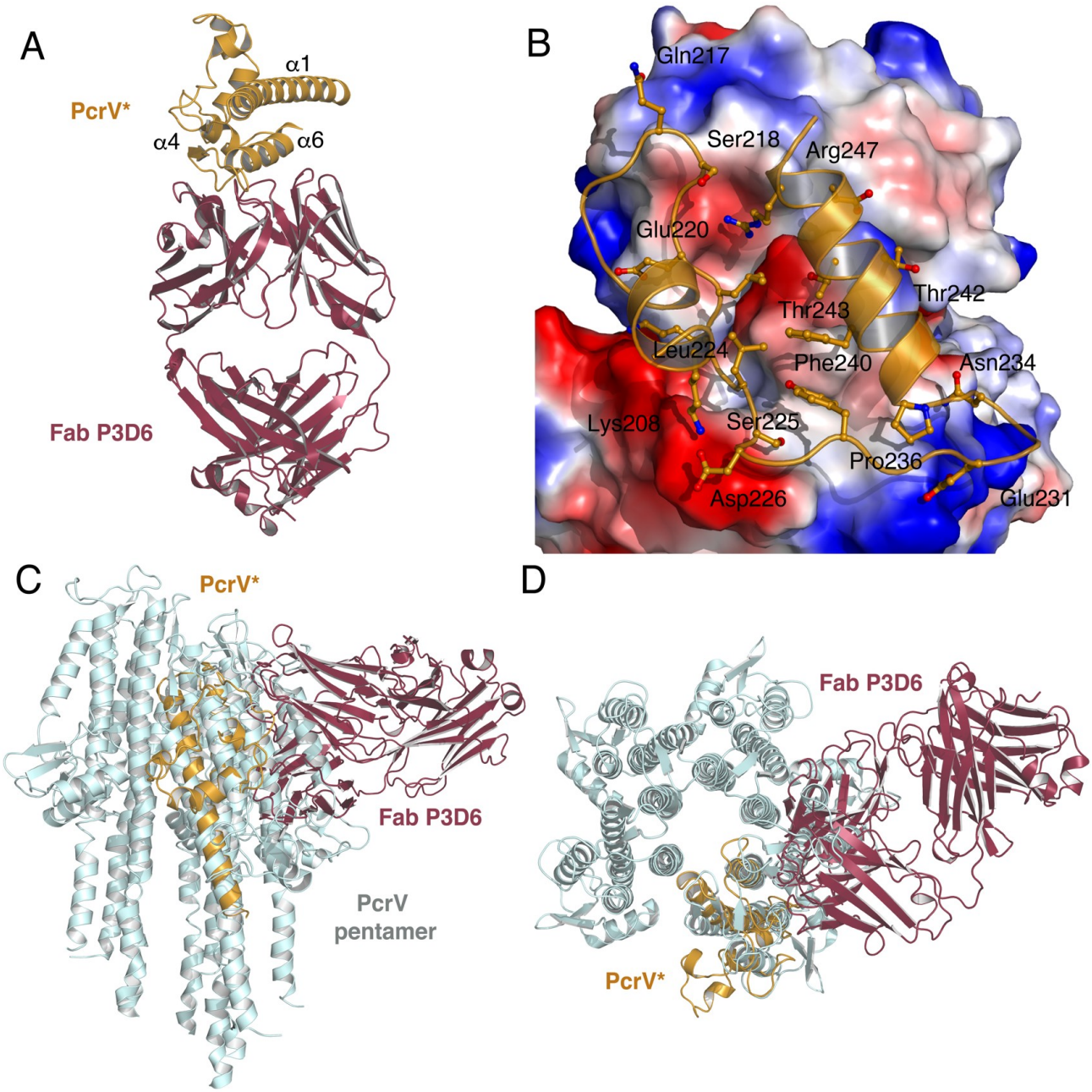

Figure 5. Structure of Fab P3D6 in complex with PcrV*. (A) Crystal structure of Fab P3D6 in complex with PcrV*. Fab P3D6 is shown in brown, while PcrV* is in orange. Contacts are made between PcrV* and an interaction platform formed by both HC and LC of P3D6. (B) Closeup of the interaction between PcrV* and P3D6, with the latter being shown as an electrostatic surface where acidic regions are shown in red, and basic in blue. Side (C) and top (D) views of the modeled PcrV pentamer, in light blue) onto which the structure shown in (A) was overlaid.

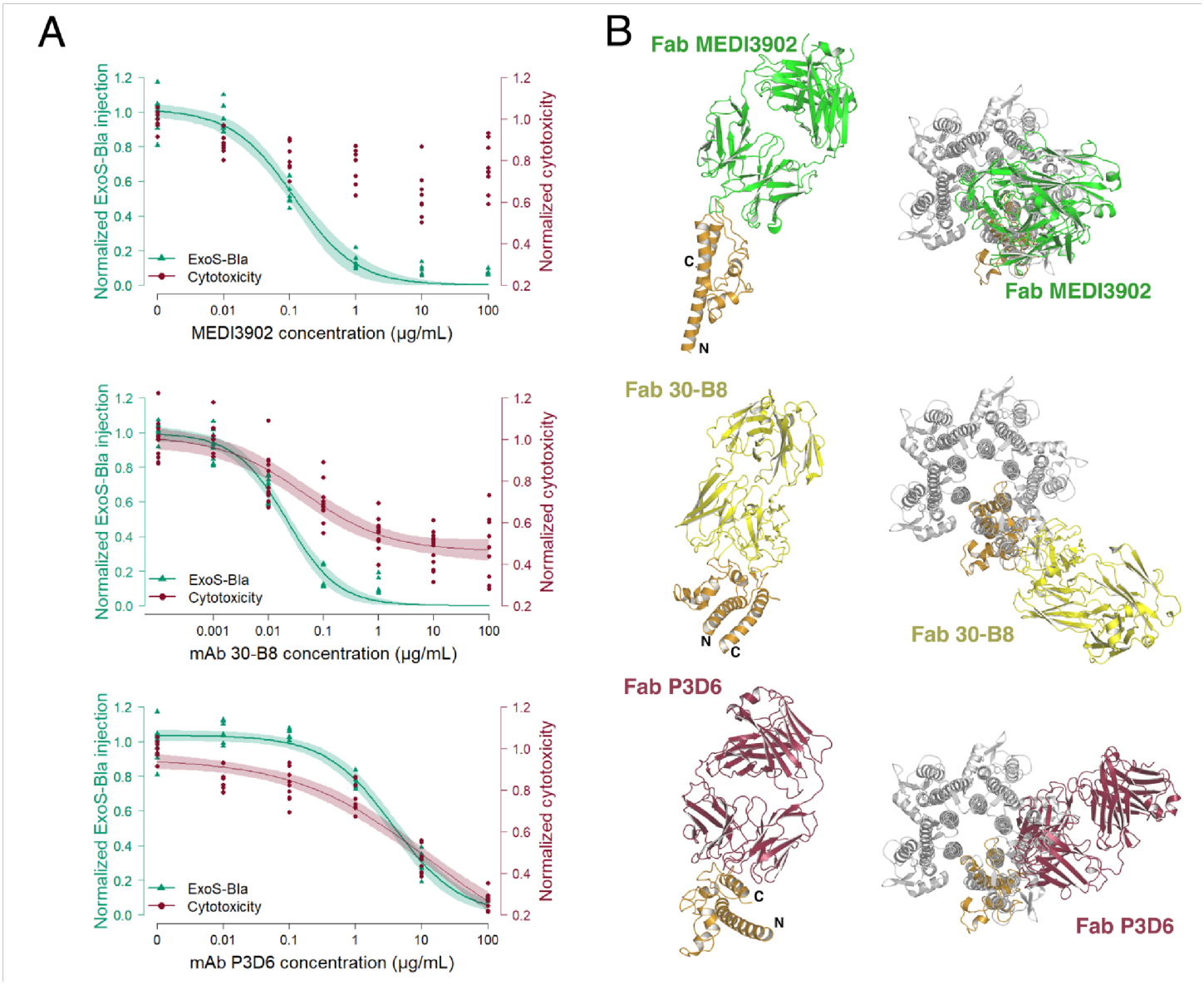

Figure 6. Functional and structural comparisons between anti-PcrV mAbs.

(A) Dose-dependent inhibition of T3SS in two functional assays reflecting toxin injection (ExoS-Bla injection) and translocon assembly (J774 macrophage cytotoxicity) for three mAbs. The circles, the dark lines and the light-colored areas represent the experimental values, the log-logistic modeled dose-response curves and the 95% confidence intervals, respectively. The Ab concentration is presented in logarithmic scale. No red curve nor red area is displayed for MEDI3902 because no dose-response could be modeled. (B) Structures of PcrV-Fab complexes in the context of a PcrV monomer, as well as of a pentamer modeled based on the cryo-EM structure of SipD (Guo and Galan 2021). The N- and C- termini of PcrV are indicated in all structures, which are referenced in the main text.

AUTHOR CONTRIBUTIONS

JMD, EF, CCM, FC, LSDD, AA, IB, VTC and FC performed experiments and analyzed the data; EF, JMD, VTC, CCM and LSDD prepared the figures; DF and YC provided the tools and materials; IA, AD and PP designed the study, analyzed the data, and wrote the manuscript. All authors participated in discussions and editing of the final version of the manuscript.

All data reported in this paper including antibody sequences will be shared by the lead contact upon request.

DECLARATION OF INTERESTS

The authors declare no competing interests.

SUPPLEMENTARY DATA FOR

Neutralizing human monoclonal antibodies that target the PcrV component of the Type III Secretion System of *Pseudomonas aeruginosa* act through distinct mechanisms

Jean-Mathieu Desveaux[1], Eric Faudry[1], Carlos Contreras-Martel[1], François Cretin[1], Leonardo Sebastian Dergan-Dylon[1], Axelle Amen[1,2], Isabelle Bally[1], Victor TardivyCasemajor[1], Fabien Chenavier[1], Delphine Fouquenet[3], Yvan Caspar[1,4], Ina Attrée*[1], Andréa Dessen*[1], Pascal Poignard*[1,5]

[1] Univ. Grenoble Alpes, CEA, CNRS, Institut de Biologie Structurale (IBS), F-38044 Grenoble, France

[2] Laboratoire d'Immunologie, CHU Grenoble Alpes, France

[3] Centre d'Étude des Pathologies Respiratoires INSERM U1100 - UFR de Médecine de Tours, 10 Bd Tonnellé, 37032 Tours Cedex

[4] Laboratoire de Bactériologie-Hygiène Hospitalière, CHU Grenoble Alpes, France

[4] Laboratoire de Virologie, CHU Grenoble Alpes, France

Supplementary Table 1. Sequence conservation of V and J regions of selected mAbs compared to germline. Percentage (%) of identity was obtained by aligning variable region sequences on IMGT database (https://www.imgt.org).

Anti-PcrV mAbs

Heavy chain	V Gene and allele	J Gene and allele	V region identity (%)	J region identity (%)	CDR3 length	Donor #
P3G9Hc	IGHV4-61*08	IGHJ6*02	92.44	91.94	18	16
P3D6Hc	IGHV3-23*01	IGHJ4*02	92.70	89.58	14	25
P5B3Hc	IGHV3-74*01	IGHJ3*02	96.88	94.00	11	25
P5E10Hc	IGHV3-21*01	IGHJ6*02	88.42	74.20	12	25
Light chain	**V Gene and allele**	**J Gene and allele**	**V region identity (%)**	**J region identity (%)**	**CDR3 length**	**Donor #**
P3G9κc	IGKV3-20*01	IGKJ3*01	94.68	100.00	10 9	16
P3D6κc	IGKV1-8*01	IGKJ4*01	96.41	97.37	11	25
P5B3λc	IGLV3-25*03	IGLJ2*01	96.10	100.00	9	25
P5E10κc	IGKV4-1*01	IGKJ4*01	95.00	100.00		25

Anti-PscF mAbs

Heavy chain	V Gene and allele	J Gene and allele	V region identity (%)	J region identity (%)	CDR3 length	Donor #
P1B7Hc	IGHV3-23*01	IGHJ4*02	97.22	91.67	13	25
P1D5Hc	IGHV4-61*02	IGHJ6*02	83.85	80.65	19	25
P1B4Hc	IGHV3-23*01	IGHJ6*02	95.14	83.87	17	25
P1F5Hc	IGHV3-23*01	IGHJ6*02	77.86	83.87	19	25
P1D7Hc	IGHV3-23*01	IGHJ4*02	96.87	93.75	15	25
P3G2Hc	IGHV4-61*02	IGHJ4*02	91.40	93.75	16	25
P3G6Hc	IGHV3-23*01	IGHJ6*02	98.61	85.48	17	25
P3G7Hc	IGHV3-72*01	IGHJ3*01	86.39	88.00	18	25
P5D5Hc	IGHV3-23*01	IGHJ4*02	96.52	93.75	13	25
P5G10Hc	IGHV4-34*01	IGHJ6*02	91.22	77.42	16	25
Light chain	**V Gene and allele**	**J Gene and allele**	**V region identity (%)**	**J region identity (%)**	**CDR3 length**	**Donor #**
P1B7κc	IGKV1-16*02	IGKJ2*01	97.13	97.14	9	25
P1D5κc	IGKV2-28*01	IGKJ3*01	94.22	100.00	9	25
P1B4κc	IGKV3-20*01	IGKJ1*01	95.04	97.14	9	25
P1F5κc	IGKV2-28*01	IGKJ2*01	95.58	89.47	17	25
P1D7λc	IGLV3-21*02	IGLJ2*01	98.56	97.37	11	25
P3G2λc	IGLV2-8*01	IGLJ2*01	94.79	88.57	10 9	25
P3G6κc	IGKV3-20*01	IGKJ2*01	99.60	89.74	11 9	25
P3G7λc	IGLV1-51*01	IGLJ2*01	88.00	91.67	11	25
P5D5κc	IGKV1-16*01	IGKJ2*01	98.20	94.29		25
P5G10λc	IGLV1-47*01	IGLJ2*01	94.73	91.67		25

Supplementary Table 2. Competition between A) anti-PscF mAbs and B) anti-PscF mAbs. The indicated IC_{50} values correspond to the concentration of competitor mAbs necessary to obtain half of the signal generated by the biotinylated mAbs without competitor. ND corresponds to a non-detectable competition.

		Detection mAbs							
		P1D8*	P1B7*	P5D5*	P3G6*	P1D6*	P1B4*	P1D5*	P5G10*
Competitor mAbs	P1D8	0,01	ND	ND	ND	ND	ND	ND	ND
	P1B7	ND	0,19	0,16	0,16	0,60	0,20	0,52	ND
	P5D5	ND	0,39	0,68	0,46	0,33	0,26	1,39	ND
	P3G6	ND	12,66	2,99	1,77	8,37	5,18	7,99	ND
	P5G10	ND	ND	ND	ND	ND	ND	ND	0,46
	P1D6	ND	15,02	0,89	1,17	1,62	1,83	5,30	ND
	P1B4	ND	2,83	0,61	2,06	7,67	1,97	5,00	ND
	P1D5	ND	14,21	0,86	0,70	3,85	0,23	0,69	ND

IC50 (µg/mL)
ND
9-20
4-8
<3

		Detection mAbs			
		P3G9*	P3D6*	P5B3*	P5E10*
Competitor mAbs	P3G9	0,98	ND	ND	ND
	P3D6	ND	0,8	0,28	ND
	P5B3	ND	2,42	0,41	ND
	P5E10	ND	ND	ND	0,51

IC50 (µg/mL)
ND
9-20
4-8
<3

Supplementary Table 3. Affinities of anti-PcrV mAbs for PcrV. The reported values correspond to the average of the measurements obtained from two independent experiments (n=2). Standard Deviations were calculated by the BLI analysis software.

IgG/His-PcrV-avitag	K_D (10^{-12}M)	K_{on} (10^2/Ms)	k_{on2} (1/Ms)	K_{off} (10^{-7}/s)	k_{off2} (10^{-3}/s)	R^2
P5B3	23.9 ± n.d	362 ± 38.2	1.2 ± 0.2	9.3 ± n.d	321.15 ± 49.7	0.9998
P3D6	736.8 ± 19	618 ± 1.5	0.4 ± 0.2	463.5 ± 12,7	12.3 ± 5.9	0.9997

Supplementary Table 4. Data collection, phasing and structure refinement statistics

DATA COLLECTION	
X-ray source (Beamline)	ESRF (ID30A-1)
Detector	Pilatus 2M
Wavelength (Å)	0.965459
Scan-range (°)	180
Oscillation (°)	0.2
Space group	$P2_1$
a (Å)	87.58
b (Å)	87.58
c (Å)	105.22
a (°)	90.00
b (°)	104.83
g (°)	90.00
Mosaicity (°)	0.129
Overall resolution (Å)	49.21-2.56
No. observed/unique reflections	176390/52157
High resolution shell (Å)	2.71-2.56
Completeness (%) (last shell)	99.5(99.2)
R_{sym} (%) (last shell)	21.7 (152.9)
$I/\sigma(I)$ (last shell)	5.02 (0.72)
$CC_{1/2}$	97.7 (31.2)
Wilson plot B-factor (Å^2)	45.86
MOLECULAR REPLACEMENT	
Phaser LLG	1032.93
R_{work}/R_{free} (%)	35.68/40.33
REFINEMENT	
Initial R_{work}/R_{free} (%)	35.68/40.33
Final R_{work}/R_{free} (%)	19.69/23.64
Final+TLS R_{work}/R_{free} (%)	20.97/23.70
STEREOCHEMICAL QUALITY	
RMS deviation, bond lengths (Å)	0.006
RMS deviation, bond angles (º)	1.266
Mean B-factor (Å^2)	46.74
No. of atoms	9052
No. of protein atoms	8614
No. of water molecules	392
Residues in most favored/allowed region of Ramachandran plot (%)	99.80

Supplementary Table 5. Bacterial strains and plasmids

***P. aeruginosa* strains**	**Characteristics**	**Reference or source**
CHAD*exoS*::*exoS-bla*	b-lactamase (bla) reporter for ExoS translocation	Verove et al., 2012
CHAD*pcrV*	Strain lacking *pcrV*	Gouré et al., 2004
PAO1D3Tox	Strain lacking toxins ExoS, ExoT and ExoY	Cisz et al., 2008
Plasmids	**Characteristics**	**Reference or source**
pIApG-*pcrV*-V1 (PAO1)	Replicative plasmid for PcrV expression, *$Leu^{6}Ala^{9}Ser^{21}Ser^{225}$	Lab collection; Simona Barzu, Lyon
pIApG-*pcrV*-V2 (CHA)	$Leu_{6}Ala_{9}Ser_{21}Arg_{225}$	Lab collection; Simona Barzu, Lyon
pIApG-*pcrV*-V3 (PA14)	$Phe_{6}Ala_{9}Pro_{21}Lys_{225}$	Lab collection; Simona Barzu, Lyon
pIApG-*pcrV*-V4 (PA103)	$Phe_{6}Gly_{9}Pro_{21}Arg_{225}$	Lab collection; Simona Barzu, Lyon
pIApG-*pcrV*-V5	$Phe_{6}Gly_{9}Pro_{21}Lys_{225}$	Lab collection; Simona Barzu, Lyon
pET15b-His-PcrV	Replicative plasmid for inducible His-PcrV expression	Nanao et al., 2003
pET22b-PscF-His	Replicative plasmid for inducible PscF-His expression	Quinaud et al, 2005
pESPRIT-His-PcrV-avitag	Replicative plasmid for inducible His-PcrV-avitag expression expression	This study
pESPRIT-His-PscF-avitag	Replicative plasmid for inducible expression His-PscF-avitag	This study

*variable residues within PcrV

Supplementary Figure 1. Dose-dependent inhibition by mAbs P5B3 and P3D6 of ExoS-Bla injection from strains expressing five PcrV variants. Inhibition of ExoSBla activity following infection of A495 epithelial cells with *P. aeruginosa* expressing the V1 (A and B), V2 (C), V3 (D), V4 (E) or V5 (F) variants, with mAbs concentration ranging from 0.01 to 100 µg/mL. The circles, the black line and the grey area represent the experimental values, the log-logistic modeled dose-response curve and the 95% confidence interval, respectively. The dashed lines represent the mean of normalized ExoS-Bla injection in the absence of antibody. The Ab concentration is presented in logarithmic scale. Monoclonal Ab P5B3 displays dose-response inhibition with the strains expressing the V1, V2, V3, V4 and V5 variants with respective IC_{50}s of 96, 206, 192, 212 and 426 µg/mL (no statistically significant difference). P3D6 (B) displays a dose-response inhibition with the strain expressing the V1 variant, with an IC_{50} of 3.7 µg/mL, significantly different from the one of P5B3 against the same variant (p-value = 0.015).

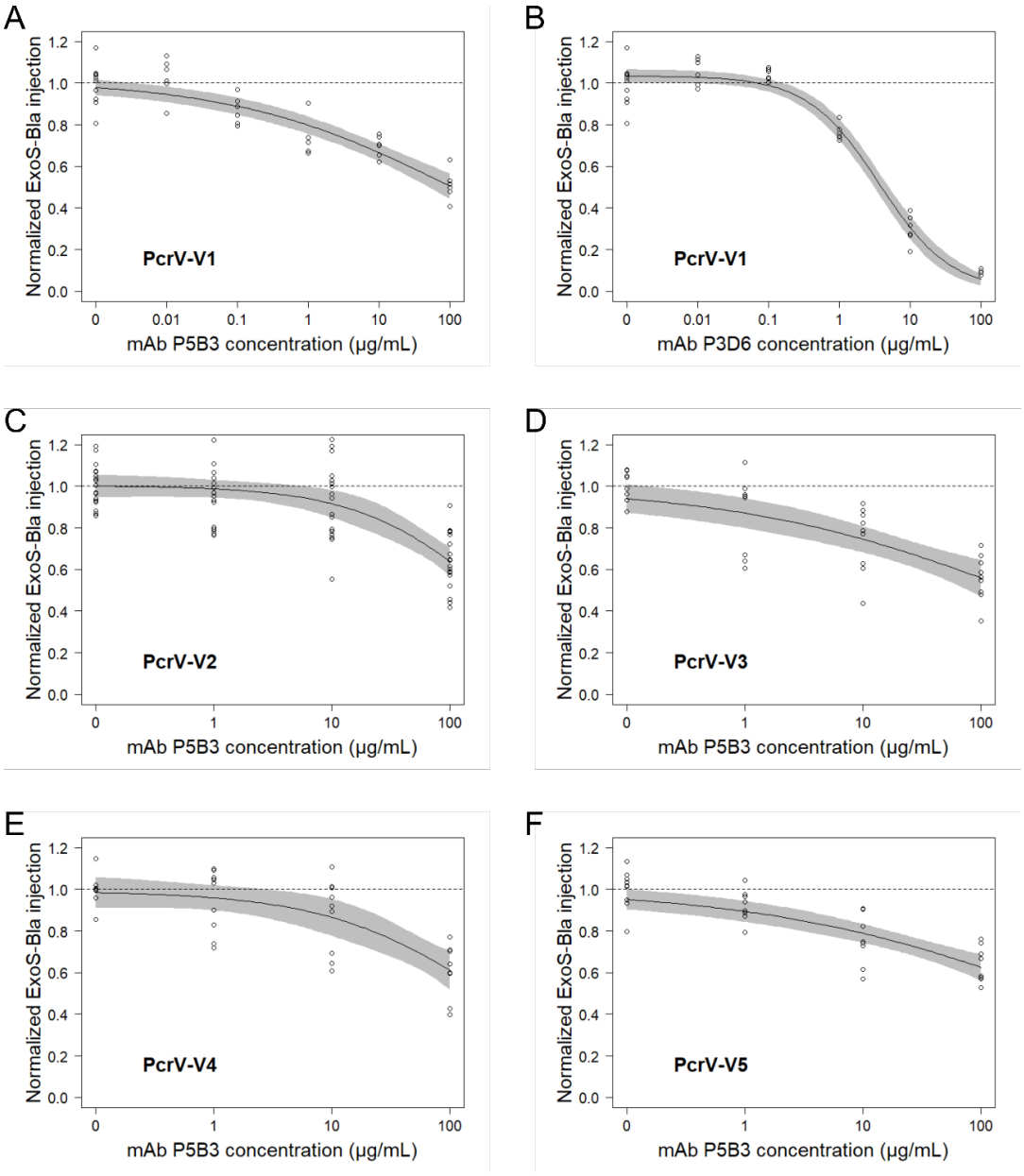

Supplementary Figure 2. Dose-dependent inhibition by mAbs 30-B8 of ExoS-Bla injection from strains expressing five PcrV variants. Inhibition of ExoS-Bla activity following infection of A495 epithelial cells with *P. aeruginosa* expressing the V1, V2, V3, V4 or V5 variants, with mAbs concentration ranging from 0.001 to 1 µg/mL. Monoclonal Ab 30-B8 displays dose-response inhibition with V1, V2, V3, V4 and V5 variants with respective IC50 of 21.3, 12.8, 11.2, 13.0, 10.5 ng/mL. The dark lines and the light-colored areas represent the log-logistic modeled dose-response curve and the 95% confidence interval, respectively. The dashed lines represent the mean of normalized ExoS-Bla injection in the absence of antibody. The Ab concentration is presented in logarithmic scale.

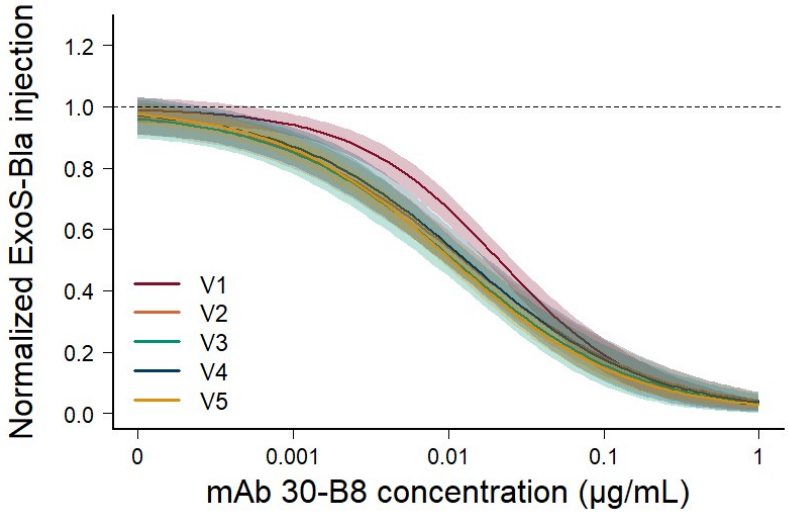

Supplementary Figure 3. Interactions between PcrV* and Fab P3D6. Chain codes correspond to: Fab HC (chain A), LC (chain C) and PcrV* (chain E). CDR H1, H2 and H3 of the heavy chain, as well as CDR L1 and L3 of the light chain, contribute to PcrV* binding. Interaction diagram generated with LigPlot+ v.2.9.9 (Lakowski & Swindells 2011, https://www.ebi.ac.uk/thornton-srv/software/LigPlus/). Hydrogen bonds are represented by green dashed lines and residues involved in hydrophobic contacts are indicated by spoked arcs.

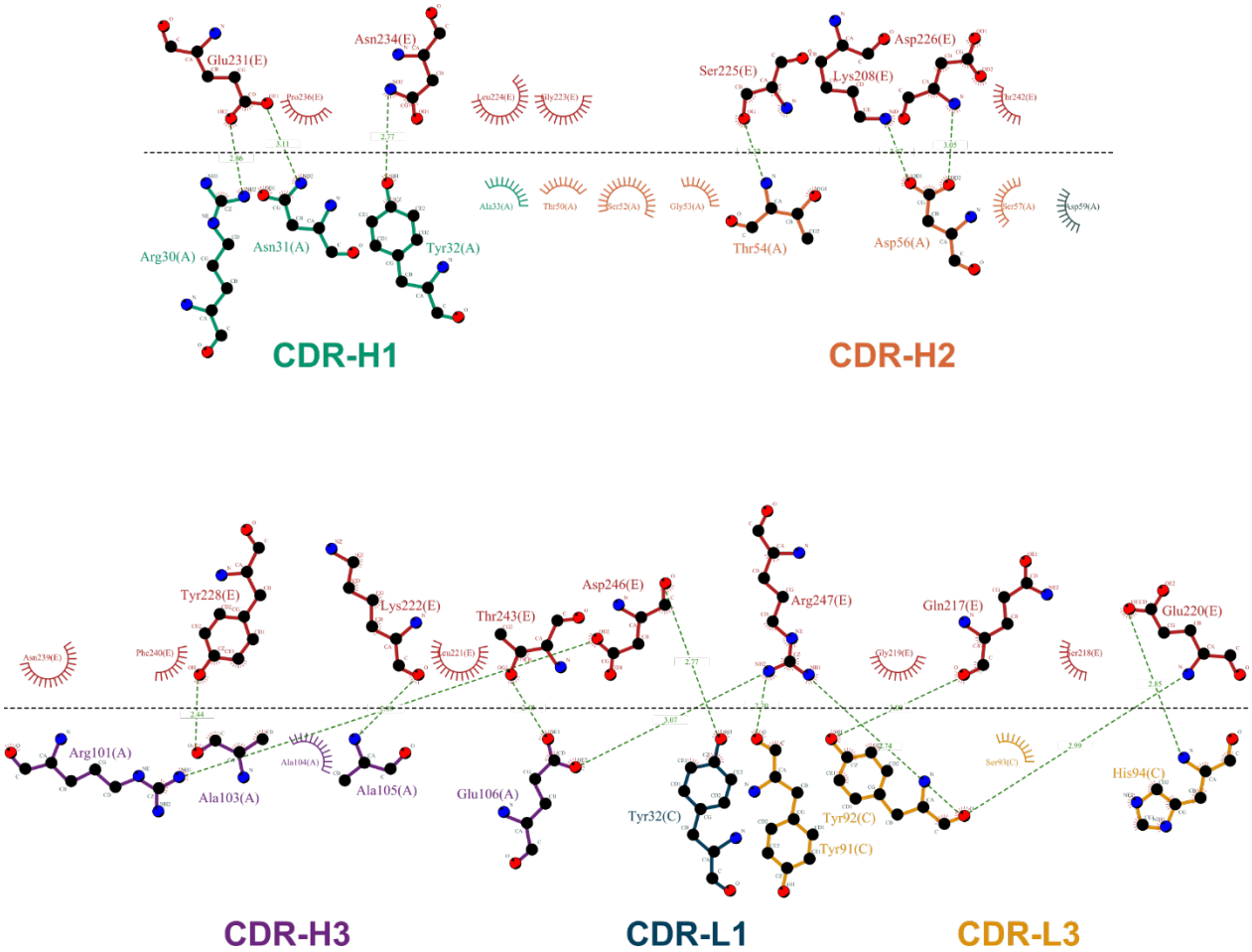

SUPPLEMENTARY REFERENCES

Cisz M, Lee P-C, Rietsch A. 2008. ExoS Controls the Cell Contact-Mediated Switch to Effector Secretion in *Pseudomonas aeruginosa*. *J Bacteriol* **190**:2726–2738. doi:10.1128/JB.01553-07

Goure J, Pastor A, Faudry E, Chabert J, Dessen A, Attree I. 2004. The V Antigen of *Pseudomonas aeruginosa* Is Required for Assembly of the Functional PopB/PopD Translocation Pore in Host Cell Membranes. *Infect Immun* **72**:4741–4750. doi:10.1128/IAI.72.8.4741-4750.2004

Laskowski R A, Swindells M B. 2011. LigPlot+: multiple ligand-protein interaction diagrams for drug discovery. *J. Chem. Inf. Model.*, **51**, 2778-2786.

Nanao M, Ricard-Blum S, Di Guilmi A, Lemaire D, Lascoux D, Chabert J, Attree I, Dessen A. 2003. [No title found]. *BMC Microbiol* **3**:21. doi:10.1186/1471-2180-3-21

Quinaud M, Chabert J, Faudry E, Neumann E, Lemaire D, Pastor A, Elsen S, Dessen A, Attree I. 2005. The PscE-PscF-PscG Complex Controls Type III Secretion Needle Biogenesis in Pseudomonas aeruginosa. *Journal of Biological Chemistry* **280**:36293–36300. doi:10.1074/jbc.M508089200

Verove J, Bernarde C, Bohn Y-ST, Boulay F, Rabiet M-J, Attree I, Cretin F. 2012. Injection of Pseudomonas aeruginosa Exo Toxins into Host Cells Can Be Modulated by Host Factors at the Level of Translocon Assembly and/or Activity. *PLoS ONE* **7**:e30488. doi:10.1371/journal.pone.0030488